Potential of CO2 capture from flue gases by physicochemical and biological methods: A comparative study

Ismael Matito-Martos, Claudia Sepúlveda, Cintia Gómez, Gabriel Acién, Julio Perez-Carbajo, José Delgado, V.I. Águeda, Conchi Maria Concepcion Ovin Ania, José Parra, Sofía Calero, et al.

Potential of CO_2 capture from flue gases by physicochemical and biological methods: a comparative study

Doi:⟨10.1016/j.cej.2020.128020⟩

Ismael Matito-Martos[a,¶], Claudia Sepulveda[b,¶,*], Cintia Gómez[c], Gabriel Acién[c], Julio Perez-Carbajo[a], J. A. Delgado [d], V. I. Águeda[d], Conchi Ania[e], J. B. Parra[f], S. Calero[a] and J. A. Anta[a]*

¶ These two authors contributed equally to this work.

[a]*Department of Physical, Chemical and Natural Systems, University Pablo de Olavide, Sevilla 41013, Spain*
[b] *Bio-innovation Centre*, Antofagasta Institute, University of Antofagasta, Chile

[c]*Department of Chemical Engineering*, University of Almería, 04120 Almería, Spain

[d]*Department of Chemical Engineering, Universidad Complutense de Madrid, 28040, Madrid, Spain*

[e]*CEMTHI (CNRS UPR 3079) Université d'Orléans, 45071, Orléans, France.*

[f]*Instituto Nacional del Carbón, INCAR, CSIC, P.O. 73, 33080 Oviedo, Spain.*

Corresponding authors*: Claudia Sepúlveda (Claudia.sepulveda@uantof.cl), Juan A. anta (anta@upo.es)

KEYWORDS: CO_2 capture, zeolites, microalgae, light efficiency

Abstract

The industrial viability of state-of-the art technologies for CO_2 capture from flue gases and their commercial valorization is analysed and compared. Our focus is on the alternative capabilities of physicochemical and biological methods, i.e., adsorption in porous commercial zeolites and biomass production by microalgae, respectively. In both cases the study is organized in two steps: first the best system for CO_2 capture is selected (type of zeolite in one case and microalgae strain in the other). Second figures about their performance at real conditions are obtained and the advantages and disadvantages of each alternative are discussed. For the physicochemical process, it is found that commercial zeolite MFI is the best choice for CO_2 capture from a typical industrial flue gas emission. Numerical simulations of dual PSA cycle at ambient conditions (pressure and temperature) provides a value of 8 kg m^{-3} bed h^{-1} and an energy compsuption of 0.987 MJ/Kg of captured CO_2. As regards the biological process, evaluation of different microalgae strains in continuous mode using low cost resources (low quality water, fertilizers, flue gases), results in *Scenedesmus* as the most promising strain. The maximal capacity of CO_2 capture determined at laboratory conditions was 0.1 kg m^{-3} broth h^{-1}, allowing to produce up to 0.06 of kg m^{-3} broth h^{-1} of biomass with a 3% maximal photosynthetic efficiency. Although this is a significantly lower value, the produced biomass is mainly composed by carbohydrates, that would lead to an overall economic yield being 0.6 €/m^3·day. These figures allow to confirm the reliability of the process at large scale. To demonstrate it, experiments were performed in a 100 m^2 pilot scale raceway reactor under real outdoor conditions. At these conditions the CO_2 capture capacity was 54 g/m^2·day (equivalent to 197 tn/ha·year) with biomass productivity values of 21 g/m^2·day (equivalent to 75 tn/ha·year) on an annual basis. On the other hand, the energy consumption approaches to 0.48 MJ/kgCO_2, lower than amines-related absorption process, of 4 MJ/kgCO_2, and zeolites adsorption.

1. INTRODUCTION

The relationship between Global Warming and increasing emissions of Green House Gases (GHG) is not more under discussion, most of the countries signing the Paris Protocol to mitigate the anthropogenic emissions of these gases.[1] Thus, countries are enforced to implement real mitigation strategies considering reduction of GHG emission both by improvement of the technology for energy production and the development of technologies for GHG capture. Among the different GHG, carbon dioxide is one of the most relevant for the larger magnitude of its emission, mainly related with energy production for fossil fuels [2]. A reduction in power consumption or improvements to combustion processes can help reducing CO_2 emissions. Alternatively, carbon capture and storage (CCS) shows great potential in diminishing the amount of CO_2 released into the atmosphere from industrial and civil combustion processes[3,4]. CCS refers to strategies for capturing CO_2 from flue gases followed by long-term storage for hundreds of years; these are capable of contributing up to 55 % to the mitigation effort[3]. Different technologies have been proposed for CO_2 capture,[5] the most conventional being based on ammines-related absorption processes,[6] other using membranes[7] or including cryogenic processes[8] to capture the CO_2 from the flue gases. A major problem related with these technologies is the large energy consumption, the difficulty to recover the CO_2 gas, and its tolerance to the corrosive conditions imposed by the flue gases composition[9]. Additionally, the utilization of porous materials for CO_2 adsorption in Pressure Switch Adsorption (PSA) processes has been also proposed.[10] This technology requires less energy and also facilitates the recovery of the CO_2 gas by using a readily available driving force such as the pressure difference between the high feed pressure for adsorption and a lower pressure for desorption. However, PSA methods still rely on the availability of materials with improved properties in terms of CO_2 adsorption capacity and selectivity. Materials that have been thoroughly studied are mainly inorganic zeolites,[11] metal organic frameworks[12], as well as the functionalization of these with room temperature ionic liquids[13] among others. It must be born in mind that whatever the CO_2 capture process is, energy consumption must remain low and, besides, the final product, in the form of a concentrated CO_2 stream, must be valorised.

As an alternative to chemical and physicochemical techniques, the utilization of microalgae for CO_2 capture process has also been proposed. This biological process has been reported to require less energy, thus it is potentially more sustainable from the environmental point of view. However, biological methods are more sensible to pollutants contained into the flue gases and their typical rate of CO_2 capture is lower than that of chemical processes.[14,15] In spite of that, they have the critical advantage of providing a final product (microalgae biomass) that would be more valuable than the CO_2 stream of the chemical and physicochemical methods, thus positively contributing to the economic sustainability of the entire process. There is a lot of studies about the application of microalgae for CO_2 capture, most of them related with the production of biofuels, all of them concluding that the reliability of the process is highly dependent on the strains tested, production scale/technology and final application of the biomass. Moreover, the large surface and the overall cost of the technology are actually bottlenecks for the commercial development of microalgae-based CO_2 capture processes.[16–19]

In the last years, the large scale production of microalgae is fast increasing mainly by two reasons: (i) the enlargement of the market as microalgae biomass is now included in more food/feed products, and (ii) the improvement of the technology allowing to increase the biomass productivity, thus reducing the biomass production costs. Some important advances includes the development of more robust strains (improved strains non genetically modified), improvement of energy utilization efficiency and mass transfer capacity on the reactors, and development of new downstream strategies and products.[20–24] These advances make the possibility of using microalgae for CO_2 capture process much more realistic today than twenty years ago, especially if combined with the treatment of other wastes as wastewater or manure.[19,25] Thus, the growth potential of microalgae-based methods can be up to 100 times faster than terrestrial plants, thus achieving productivities of 100 tn/ha·year. To achieve these figures, large amounts of nutrients are required: for each tonne of biomass produced, it takes up to 2 tnCO_2, 100 kgN and 10 kgP. This can actually be provided by flue gases and wastewater.[20] Additionally, large surfaces and adequate environmental conditions (light, temperature, etc..) are required, factors such as pH, temperature and light intensity have a great influence on the growth dynamics of microalgae as do the nutrients [26].

The aim of this work is to re-think the CO_2 capture process taking into account the actual technology available in order to determine the real suitability of novel processes at different scales. We will focus our study on zeolite-based CO_2 adsorption (physicochemical process) and microalgae-based CO_2 capture (biological process). In both cases, a common composition of flue gas, with varying CO_2 concentrations, typical of industrial combustion activities, have been considered. On the one hand, a combination of molecular simulation, numerical modelling of the continuous PSA process and equilibrium adsorption experiments has been used to assess the potentiality of CO_2 capture of the physicochemical method. On the other hand, a 100 m^2 pilot scale raceway reactor has been used to evaluate the capability of the biological process under real outdoor conditions in terms of biomass production and CO_2 capture efficiency. In both cases a previous screening has been done to select the optimum zeolite (physicochemical process) and the optimum microalgae strain (biological process). Figures from the reactor experiment allows to evaluate the energy consumption and cost of the biological process, and to compare it with their physicochemical counterpart. Considering final applications of the biomass the suitability of both processes at commercial scale is finally discussed.

2. MATERIALS AND METHODS

2.1. Theoretical determination of adsorption isotherms in zeolites

Adsorption isotherms were computed using Monte Carlo simulations in the Grand Canonical ensemble (GCMC). In this ensemble, the average value of the temperature, the volume, and the chemical potential remain fixed. The chemical potential directly relates to fugacity, and then fugacity to pressure by the fugacity coefficient through the Peng–Robinson equation of state.[27] The MC trial moves employed were translation, rotation, and reinsertion of gas molecules, swap from the reservoir, and identity change for mixtures.[27] Results were obtained after running 10^3 equilibration and $5 \cdot 10^3$ production cycles, respectively. In the case of water, up to $2 \cdot 10^6$ production cycles were used in order to equilibrate some particular pressure points. The number of Monte Carlo steps per cycle equals the total number of molecules in the system with a minimum of 20. Described simulations are performed using the simulation code RASPA.[28,29]

Atomic interactions were taken into account by electrostatic interactions, considered by using Coulombic potential and Ewald summations; and van der Waals interactions, described by 12-6 Lennard-Jones potential.[27] In both cases, the cutoff distance is set to 12 Å, where the interactions are truncated and shifted with no tail corrections applied. These simulation conditions are commonly used to study adsorption in confined systems.[30,31] Adsorbate molecules were all considered rigid, as they are already reported for CO_2,[32] N_2,[33] O_2,[33] and H_2O.[34] Details and parameters of the interaction model used for these molecules can be found in the Supporting Information (**Section A**, **Table S1**)

Six widely employed zeolites with different geometry and topology were selected for this work (i.e. BEA, FAU, FER, ITQ-29, MFI, and MOR). Most of them are commercially available and used for different gas separations. We use a pure-silica version of these zeolites, considering them as rigid frameworks as it is well-known that the effect of zeolite flexibility is usually small in adsorption studies.[35] A representation of the grid surface energy of the selected materials is presented in **Fig. S1**. A description of the morphology and crystalline structure of these zeolites as considered in the modeling is also included in the Supporting Information (**Section B**, **Figure S2**, **Table S2**).

The insertion of molecules using Monte Carlo can take place in cavities or channels experimentally accessible only for some small adsorbates, such as H_2 or H_2O. To avoid this artificial insertion of molecules and reproduce experimental behavior, these cavities need to be carefully blocked.[36,37] As in previous works, we use Monte Carlo and Molecular Dynamics (MD) simulations to identify these inaccessible cavities.[38,39] First we identify energetic preferential adsorption sites for the molecules using MC, and then MD informs about the diffusion of the molecules. These sites from which molecules are unable to escape after 0.15 ns were properly blocked. In RASPA, the blockage is implemented using a list of geometric descriptions of the inaccessible volumes that are automatically considered as an overlap in MC simulations. Using this methodology, sodalites in FAU and ITQ-29 and *y*-axis channels in FER were blocked for all the molecules under study (except for H_2O) due to narrow access windows do not allow diffusion of these molecules.

2.2 Experimental determination of adsorption isotherms in MFI zeolite

Experimental equilibrium gas adsorption isotherms for pure gases (CO_2 and air) and for a mixture of 10 % CO_2 in air were recorded on pure silica MFI zeolite at room temperature using a volumetric analyser (Micromeritics) in the pressure range between 10^{-2} and 120 kPa. The zeolite was outgassed under dynamic vacuum at 623 K (1K/min) overnight before the gas adsorption measurements. All the gases were supplied by by Air Liquide with an ultra high purity (i.e., 99.995%). Pure silica MFI zeolite was supplied by Institute of Chemical Technology, CSIC, Spain.

2.3 Pressure Swing Adsorption (PSA) simulations

Typical flue gas at ambient conditions mixture (0.75 N_2, 0.10 CO_2, 0.11 O_2, and 0.032 H_2O at 298 K and 1 bar) was considered in the PSA simulations. A simple Skartrom PSA cycle in *isothermal conditions* was first considered to compare the separation performance of the different 6 zeolites simulated in **Section 2.1**, because the model resolution is quite faster than with more complex cycles. Although industrial PSA processes usually operate adiabatically, the isothermal conditions can be achieved if the bed diameter is reduced and heat exchange rate between the bed and the surroundings is increased. A detailed cycle description is presented in **Fig. S3** in the Supporting Information. Operating conditions and model parameters are given in **Table S3**. The high pressure (P_H) of the cycle is defined to 1 bar to avoid the energy consumption on compressing the feed gas. A low pressure (P_L) of 0.1 bar is used as it is a typical limit considered for practical application of PSA technology.[40,41] It is also assumed that the adsorbent crystals are agglomerated in pellets, and that mass transfer between gas and adsorbent is controlled by macropore diffusion, neglecting intracrystalline resistance.[42]

The multicomponent adsorption isotherms for the PSA simulations were obtained by applying the Ideal Adsorption Solution Theory (IAST)[43] , previously obtained by GCMC simulations. Isotherms were fitted with the Langmuir equation.[44] Details of the simulations and the fit are summarized in the Supporting Information (**Section C**)

In order to improve the yield of the CO_2 separation predicted in the previous PSA Skarstrom cycle, a dual-PSA cyle with three equalization steps in *adiabatic conditions*, with MFI zeolite as adsorbent in the bed was also implemented.[45] The dual-PSA cycle

includes two coupled PSA cycles where one cycle increases the CO_2 concentration to an intermediate value (rectifying PSA) and the other increases further the CO_2 concentration up to the desired specification (stripping PSA). The same PSA cycle has been used for each one of the coupled cycles. The individual PSA cycle is presented in **Fig. S4a** in the Supporting information. Light product and tail gas are obtained at 1 bar. The way of coupling the individual PSA cycles for the dual configuration is presented in **Fig. S4b**. Other parameters used in the simulations (except gas velocities) are given in **Table S3**. To model the effect of temperature on the adsorption isotherms, the pure adsorption isotherms of all the components in MFI have been obtained by GCMC simulation, and they have been fitted with the temperature dependent Langmuir model ($q = K_{H0} \exp(-\Delta H/RT)\, p / (1+b_0 \exp(-\Delta H/RT)\, p$). A comparison between the fitted isotherms and the molecular simulation data is presented in **Fig. S6**, and the obtained Langmuir parameters are presented in **Table S6**.

2.4 Microorganisms and culture media

Different microorganisms, microalgae and cyanobacteria, were preselected according to previous experience and the literature; more than 40 reference works being reviewed in depth for that. Only robust strains suitable for large-scale production under non-optimally controlled conditions were selected (**Table S7** in the Supporting Information). Some of the microorganisms were already available at the University of Almeria whilst others were obtained from official culture collections, mainly from the Culture Collection of Algae and Protozoa (Oban, Scotland). Inoculum from all the strains were kept under controlled conditions in 1 L flasks, at 20 °C, under constant illumination at 200 $\mu E \cdot m^{-2} \cdot s^{-1}$ provided by fluorescent lamps, with constant aeration at 0.1 v/v/min with no CO_2 supply in a standard Arnon culture medium. The standard culture medium was prepared using freshwater and Mann & Myers medium prepared using fertilizers (0.14 $g \cdot L^{-1}$ $K(PO_4)_2$, 0.18 $g \cdot L^{-1}$ $Mg(SO_4)_2$, 0.9 $g \cdot L^{-1}$ $NaNO_3$, 0.02 $mL \cdot L^{-1}$ Welgro, and 0.02 $g \cdot L^{-1}$ Kalentol), it being autoclaved at 121 °C for 15 minutes only for laboratory trials. The inoculum cultures were monitored by microscopic observation using a Leica CME microscope 40X/0.65 to verify non-contamination.

2.5 Laboratory photobioreactors

Experiments were performed in bubble-column photobioreactors (~ 300 mL) aerated at 0.2 v/v/min with pH controlled at 8.0 by on-demand injection of real flue gas (from a diesel boiler). The temperature inside the reactors was kept at 25ºC by controlling the temperature of the chamber in which the reactors are located. A total of 15 bubble-column reactors were used and each experiment was tested in triplicate. The reactors are illuminated artificially using fluorescent lamps that are automatically turned on or off to simulate the circadian solar cycle. Irradiance on the reactors surface (I_o) varied throughout the day from zero to 1200 $\mu E \cdot m^{-2} \cdot s^{-1}$ at noon - using these values, a mean irradiance for the light period (I_{light}) of 780 $\mu E \cdot m^{-2} \cdot s^{-1}$ was obtained. On a 24 h basis, the mean irradiance on the reactor surface (I_{day}) was 390 $\mu E \cdot m^{-2} \cdot s^{-1}$.

Experiments were performed in continuous mode. For this, we used inoculum from previous cultures developed in flasks but without pH control and under continuous illumination at 200 $\mu E \cdot m^{-2} \cdot s^{-1}$. The volume of inoculum supplied to the reactors at the beginning of the experiment was 10% of the total culture volume in the bubble column. Once the reactor was inoculated, it was operated in batch mode for 5 days, after that it was operated in semicontinuous mode at 0.3 day^{-1} dilution rate (medium inlet and harvesting are performed during illuminated period), till steady state was achieved (at least two times the hydraulic retention time). During the experiments the cultures were daily monitored measuring the biomass concentration and the fluorescence of chlorophylls. Water evaporation was compensated for each day with distilled water to avoid changes in conductivity or of any nutrient in the culture broth. At the end of the experiment, when a steady state was achieved, the entire culture was harvested and the biomass was stored for biochemical composition analysis.

2.6 Outdoor raceway

The raceway reactor is located at the “Las Palmerillas” Research Centre, 36° 48′N–2° 43′W, part of the Cajamar Foundation (Almería, Spain). The reactor consists of two 50 m long channels (0.46 m high × 1 m wide), both connected by 180° bends at each end, with a 0.59 m^3 sump (0.65 m long × 0.90 m wide × 1 m deep) located 1 m along one of the

channels.[46] A paddlewheel system was used to recirculate the culture through the reactor at a regular velocity of 0.2 $m \cdot s^{-1}$, although it can be increased up to 0.8 $m \cdot s^{-1}$ by manipulating the frequency inverter of the engine. The pH, temperature and dissolved oxygen in the culture were measured using appropriate probes (5083 T and 5120, Crison, Barcelona, Spain), connected to an MM44 control-transmitter unit (Crison Instruments, Spain), and data acquisition software (Labview, National Instruments) providing complete monitoring and control of the installation. The pH of the culture was controlled at 8.0 by on-demand injection of flue gas (from a diesel boiler), whereas temperature was not controlled; it ranged ±5ºC with respect to the daily mean air temperature, which varied from 12ºC in winter to 28ºC in summer. The raceway reactor was inoculated and operated in batch mode for one week, after which it was operated in semi-continuous mode at 0.2 day^{-1} at a culture depth of 0.15 m. Only samples from steady-state conditions were used. Evaporation inside the reactor was compensated by the daily addition of fresh water.

2.7 Analytical methods

The cultures were examined daily under a microscope, an Olympus CH20 (Olympus Corp., USA), to evaluate the cell status and to detect possible contamination. Images of the cultures were photographed for further use. Absorbance and turbidity were measured daily to monitor the evolution of the cultures. The dry weight biomass concentration (C_b) was measured by filtering 100 ml of culture through 1 µm filters and drying it at 80ºC in an oven over a 24 h period; this measurement was performed at the end of the culture. The dry weight biomass concentration values during the batch experiments were calculated from absorbance/turbidity measurements using the correlation obtained at the end of the batch culture. Biomass productivity was calculated as the product of the biomass concentration by the imposed dilution rate. The cell status was checked daily by measuring the chlorophyll fluorescence (F_v/F_m) ratio with a fluorometer (AquaPen AP 100, Photon System Instruments, The Czech Republic). For this, the cells were adapted to the dark for 15 minutes prior to measurement. Absorbance in the visible range (400-700 nm) was measured daily using a double-beam Helios Alpha spectrophotometer and the extinction coefficient (*Ka*) was calculated by dividing the average absorbance value by the biomass concentration (*Cb*) and the cuvette's light path (*d*)): K_a = Abs /(C_b d). The average

irradiance inside the culture (I_{av}) was calculated as a function of the irradiance at the surface (I_o), the biomass extinction coefficient (K_a), the biomass concentration (C_b) and the light path inside the reactor (d):[47]

$$I_{av} = \frac{I_{light}}{K_a \cdot C_b \cdot p} \cdot \left(1 - \exp\left(-K_a \cdot C_b \cdot p\right)\right) \quad (1)$$

Because mean daily values were considered, irradiance during the light period (I_{light}) was used as the irradiance on the reactor surface to calculate the mean daily irradiance. The Quantum yield (Ψ_E) is defined as the amount of biomass generated by a unit of radiation (usually a mole of photons) absorbed by the culture. Since this represents the ratio of biomass generation to absorbed photon flux, it can be calculated using[48]

$$\Psi_E = \frac{P_b}{F_{vol}} \quad (2)$$

The photon flux absorbed through the reactor volume (F_{vol}) is calculated from the average irradiance on a culture volume basis using[48]

$$F_{vol} = I_{av} \cdot K_a \cdot C_b \quad (3)$$

The photosynthetic efficiency (PE) is the fraction of energy fixed into biomass as a function of the combustion heat of the biomass that was considered constant (Q_b= 20 MJ/kg)[48]

$$PE = \frac{P_b \cdot Q_b}{F_{vol}} \quad (5)$$

Freeze-dried biomass taken at the end of the batch culture was analysed. Lipids were determined gravimetrically from an extract obtained with chloroform:methanol (2:1) (v/v).[49] The protein content was determined using the modified Lowry method.[50] The moisture content was determined by weight losses after 24 h at 80ºC, whereas the ash content was determined by calcination at 550ºC for 6 h. The carbohydrate content of the biomass was determined as the difference remaining from 100% after taking away the protein, lipid and ash content.

3. RESULTS

3.1 CO_2 adsorption capacity of commercial zeolites: equilibrium properties and materials screening

The adsorption loadings in BEA, FAU, FER, ITQ-29, MFI, and MOR zeolites at near ambient conditions (298 K; and 1, 2 and, 10 bar) was obtained by GCMC simulation for three different typical flue gas mixtures (N_2 75%; CO_2 5%, 10%, and 15%; H_2O at saturation conditions; and O_2 up to complete the mixture). **Fig. 1** shows the gas uptakes as a function of the total pressure of the system. We can observe that the inclusion of water is almost negligible in all structures, as could be expected due to the pure-silica nature of the used materials. Competition of water with the rest of adsorbates is unfavored by the hydrophobic character of material and also due the fact that is the smallest molecule under study (kinetic diameter of around 2.6 Å).[51,52] Oxygen, is also almost displaced from adsorption by the other molecules, whatever is the concentration of CO_2 in the mixture. Again, the size (i.e. kinetic diameter of 3.467 Å) and the low polarity of this molecule (quadrupole moment of ca. 0.39 D Å)[51,52] difficult its competition with the other gases. The overall performance strongly depends on the CO_2 fraction in the mixture, that is increased from 0.05 to 0.15 while the fraction of N_2 is fixed at 0.75. In the case of the lower concentration of CO_2, N_2 prevails over CO_2 in almost all the zeolites. However, as soon as the CO_2 fraction is increased to 0.10, this molecule is able to displace N_2 from the main adsorption sites of the frameworks. Both molecules have similar kinetic diameters and the higher quadrupole moment of CO_2 probably makes the difference between them (4.30 D Å and 1.52 D Å, for CO_2 and N_2 respectively). This effect is less visible in FAU, the structure with the highest pore volume, because there is almost no competition for the available space at our pressure conditions. This is supported by the low total loading in this structure, being in the range of the other two structures with the lowest pore volume and surface area (i.e. MOR and FER). Another interesting exception is the low reduction in N_2 uptake in MOR while increasing CO_2 mixture fraction. As we say, CO_2 displaces N_2 from the main adsorption sites, but this is not the case of the additional adsorption sites in MOR, where CO_2 is rove? to not commensurate well.[30] CO_2 and N_2 Average Occupation Profiles (AOPs) for the three different gas mixture compositions at the highest pressure in MOR zeolite

(**Fig. S7**) reveals that while CO_2 is always adsorbed in the main channels, N_2 migrates from the main channels to the side pockets in which it almost does not compete with CO_2.

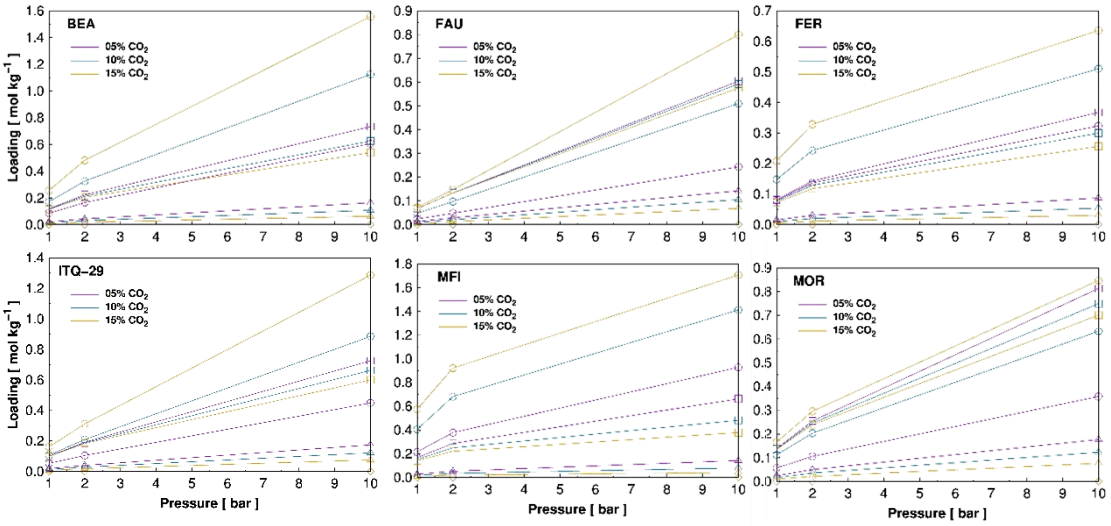

Figure 1. Adsorption loading of N_2 (squares), CO_2 (circles), O_2 (triangles), and H_2O (diamonds) in BEA, FAU, FER, ITQ-29, MFI, and MOR zeolites at room temperature and 1,2, and 10 bar of pressure. The color line indicates the fraction of CO_2 in the gas mixture.

To make a deep insight in the performance in the different zeolites, **Fig. 2a** collects the CO_2 loadings from the computed adsorption isotherms for the mixture containing 10 % CO_2 in dry air. Among all the zeolites, MFI exhibits the highest uptake for all the pressure range. Loadings of 0.4, 0.7, and 1.2 mol kg^{-1} are obtained at 1, 2, and 10 bar of pressure, respectively. Adsorption values are not very high due the relatively low working pressures, but the adsorbed fraction of CO_2 (color graduation) is increased from 0.10 in the bulk mixture to more than 0.7, indicating a very high selective capture towards CO_2. The AOPs of CO_2 in this structure (**Fig. S8**) show a strong adsorption of CO_2 in the intersections of the straight channels parallels to the y-axis and the zig-zag channels on the xz-plane. Molecules seem to commensurate well in these adsorption sites, allowing this structure to show the best performance among the studied zeolites, both in terms of uptake and preferential adsorption. From Fig. S8 it can be also observed how zig-zag and parallel channels are progressively filled from the lowest to the highest pressure.

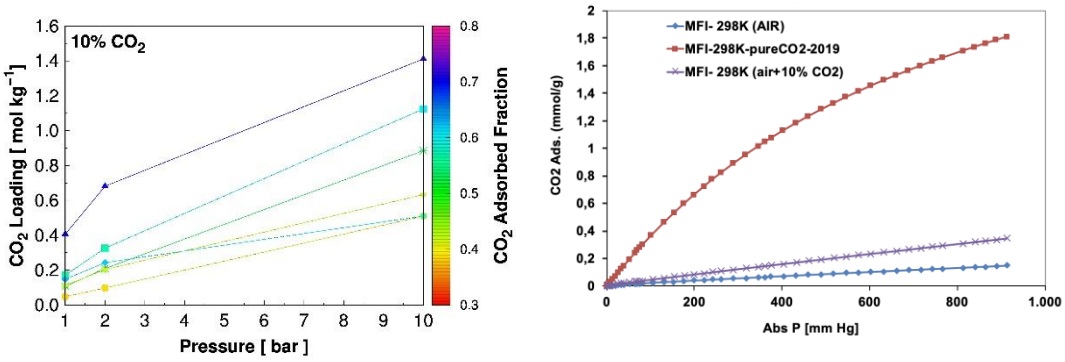

Figure 2. (A) Computed CO_2 adsorption loadings in BEA (squares), FAU (circles), FER (circles), ITQ-29 (asterisks), MFI(triangles), and MOR(diamonds) zeolites at room temperature and 1, 2, and 10 bar of pressure loadings for a mixture containing 10 % CO2 in dry air. The color code shows the CO_2 adsorbed fraction. **(B)** Experimental adsorption isotherms for MFI zeolite at room temperature for pure CO_2, synthetic air and a mixture containing 10 % CO_2 in dry synthetic air. []

BEA zeolite shows noticeably reduced CO_2 loadings compared to MFI, except at 10 bar in which pressure it reached ca. 1 mol kg^{-1}. The slightly widest system of channels explains the lower adsorption. Adsorbed molar fractions of CO_2 are also quite lower, with values between 0.6 and 0.7. The ability of the rest of zeolites to selectively capture CO_2 is even worse o more limited o more restricted, barely increasing adsorbed fractions above 0.5 and showing uptakes of less than 0.3 mol kg^{-1} at intermediate pressure. In some structures (i.e. FAU and ITQ-29), high available pore volume and cage-type topology hinder the fitting of the molecules inside them. On the other hand, the existing preferential adsorption sites in MOR for N_2, previously described, reduce the CO_2 selective capture, despite having similar pore volume, surface area and channels diameters than BEA.

In order to validate the GCMC predictions, adsorption experiments for the best performing MFI zeolite were carried out. Equilibrium adsorption isotherms for pure CO_2, synthetic air and a mixture containing 10 % CO_2 in dry synthetic air are shown in **Fig 2b.** The volumetric equipment used does not allow to discriminate the uptake corresponding to carbon dioxide in the mixture, for which the adsorption isotherm of synthetic air was also measured to estimate the contribution of nitrogen and oxygen to the adsorption of the mixture. As seen, the total amount of gas adsorbed for the mixture of 10% CO_2 in air at

atmospheric pressure is about 15.3 g/Kg zeolite (0.35 mol/Kg), which is in good agreement with the amount computed for this zeolite at 1 bar. This experimental estimation is also in line with the IAST prediction for a mixture of 10% CO_2 in air evaluated from the experimental adsortpion isotherms of air and pure CO_2 (11.4-17.2 g/kg).

3.2 CO_2 adsorption capacity of best performing zeolite: PSA estimations

To compare the performance of each of the studied zeolites in a PSA industrial cycle, we have employed the so-called "Bed Capacity Factor" (BCF) to compare the PSA performance of each structure when using the Skarstrom cycle.[42] This parameter is defined as the adsorption capacity of the column utilized at the end of adsorption step (ADS in **Fig. S3**, incipient breakthrough of the adsorbate) under cyclic steady state operation relative to the maximum capacity of the column under feed gas conditions. For the same operating conditions, the lower this parameter is the better is the PSA performance because the process is able to remove a higher amount of heavy adsorbate from the light product (rich in weak adsorptive). The advantage of BCF parameter compared to others is that it considers simultaneously the effect of the most important variables that determine separation (working capacity, adsorption rate and selectivity). For a single PSA cycle at *isothermal conditions* we obtained the following BCF values: MFI = 0.21; BEA= 0.53; FER = 0.56; MOR = 0.68; ITQ-29 = 0.80; FAU = 0.99. These results are in close agreement with the previously obtained results from GCMC simulations (**Section 3.1**) and confirms that MFI offers quite better performance than the rest of structures for CO_2 capture and separation from the flue gas.

On these grounds, the MFI zeolite is chosen to simulate the PSA dual cycle with three equalization steps at *adiabatic conditions*. As mentioned above, this type of arrangement improve the yield of CO_2 separation in industrial processes. The design specifications of the dual-PSA cycle have been defined as a CO_2 purity in the heavy product above 95% and CO_2 recovery above 90% (calculated as global results for the two coupled cycles). The feed gas velocities of both cycles have been used as input variables to achieve the desired design specifications, resulting in a feed gas velocity of 0.0452 m s^{-1} for the rectifying cycle (PSA I) and 0.11 m s^{-1} for the stripping cycle (PSA II). A flowsheet with the molar flow rates and

stream compositions of the designed dual cycle is shown in **Fig. S4b**. The performance parameters of each individual cycle and the global ones for the dual cycle are presented in **Table 1**. A CO_2 productivity of **8.24 kg/m^3/h** is estimated. The energy requirement for evacuation steps has been calculated assuming isoentropic compression with efficiency of 60%. From **Fig. S4b**, it is observed that practically dry CO_2 is obtained as final product. This is an advantage (apart from the possibility of treating a humid gas) because further drying of CO_2 is not necessary for using it in other applications.

Table 1. Performance parameters of the designed dual-PSA cycle

	PSA I	PSA II	DUAL PSA
CO_2 purity, %	35.400	95.010	95.011
CO_2 recovery, %	91.870	80.070	90.040
CO_2 productivity, $kgCO_{2\ captured}/m^3_{bed}/h$	1.140	8.550	8.240
Energy requirement, $MJ/kgCO_{2\ captured}$	0.589	0.252	0.987

3.3 Biomass production and photosynthetic efficiency by microalgae and strain screening

The first step in the use of microalgae for CO_2 capture is the selection of the right strain. A lot of microalgae and cianobacteria strains has been investigated at this respect, in most of the cases performing batch cultures, others providing continuous light, and finally using non real flue gases. To obtain reliable figures for further scale-up processes the conditions at which the strains are evaluated must be as close as possible to that prevailing at outdoor. Here, the performance of ten previously reported microalgae/cyanobacteria has been evaluated. **Fig. 3** shows that the different microalgae have largely different potential. *Scenedesmus* was the most productive, with values up to 1.6 g/L·day, whereas *Nostoc* and *Spirulina* were the less productive, with productivities below 0.5 g/L·day (**Fig. 3A**). *Scenedesmus* strain is widely reported under outdoor production conditions, including in CO_2 capture processes, as it has demonstrated itself to be robust and suitable for outdoor production, even in non-optimal raceway reactors or using wastewaters as the nutrient source [53,54]. In general cyanobacteria shows a lower performance that microalgae. These values are the maximal ones because they were obtained, although under simulated outdoor

conditions, in a well-controlled and favourable environment. The obtained figures compare well with other previously reported. Thus, using Anabaena up to 1.0 g/L·day of captured CO_2 was obtained at laboratory scale, it being mainly accumulated at released exopolysaccharides.[55] In terms of photosynthetic efficiency (PE, Eq. (5)) an analogous trend is observed because the light provided was the same for all the experiments and the light utilization is proportional to the biomass productivity (**Fig. 3B**). Crucial information in this figure is the final values, as under optimal laboratory conditions the PE can be so high as 3.0 %, much higher than that found in higher plants of 1%. These figures justify the high potential of microalgae to efficiently use the sunlight to capture CO_2 and to transform it into valuable biomass. In this respect, it has been reported that up to 200 tn/ha·year of CO_2 could be captured by microalgae.[19]

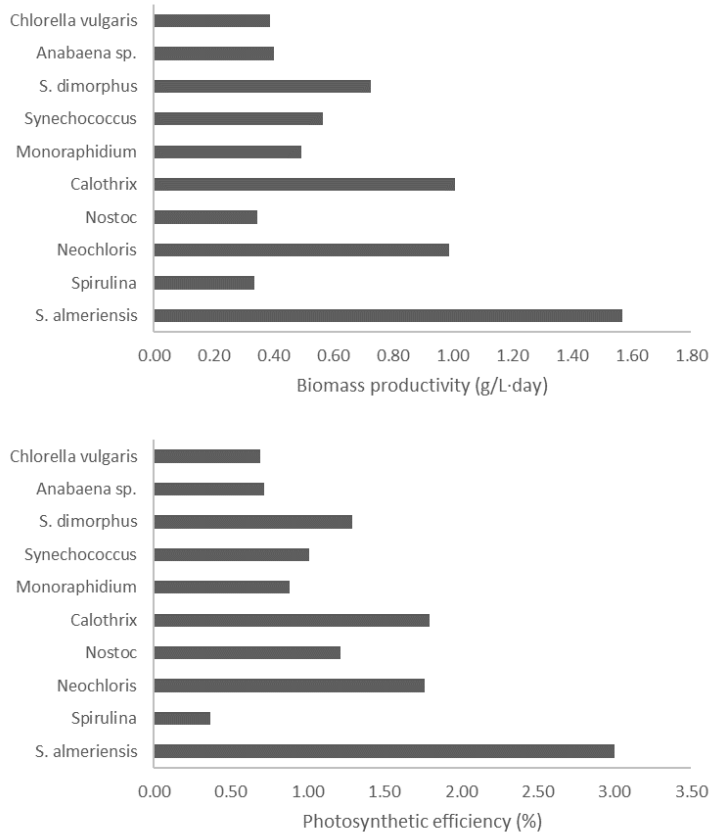

Figure 3. Biomass productivity **(A)** and photosynthetic efficiency **(B)** of microalgae strains evaluated at laboratory scale.

To analyse the real figures about CO_2 capture and how it is transformed into valuable products the theoretical CO_2 fixation rate and biochemical composition of produced biomass were determined (**Fig. S9** in the **Supporting Information**). Theoretical CO_2 fixation rate correspond to the amount of CO_2 fixed as biomass on the basis of biomass productivity and total carbon content of the biomass (ranging from 0.40 to 0.51% d.wt., data not shown). In addition to this value the net CO_2 fixation rate can be larger if the total carbon content of the biomass increases, but it is not modified too much if the cultures are operated at continuous mode, or if the CO_2 is additionally absorbed into the liquid as dissolved inorganic carbon. At laboratory scale these effects are not relevant. Hence, to consider only the net amount of CO_2 fixed as biomass is a valid approximate value. Results confirm that *Scenedesmus* is the most promising strain, showing values up to 2.5 g/L·day, much higher than that obtained when using *Nostoc* or *Spirulina* strains (**Figure S9A**). In terms of biochemical composition carbohydrates and proteins were the most relevant fractions, the lipids content being always lower than 20 %d.wt., except in the case of *Neochloris* that shows a lipids content of 26 %d.wt. (**Figure S9B**). *Neochloris* is a small microalga that accumulates large amounts of lipids, up to 50% under non-growing conditions [56]. This strain has been widely reported as a potential biofuel source as it is even able to grow in wastewaters [57,58]. In the case of *Scenedesmus* the percentage of carbohydrates was really high, up to 53 %d.wt., but it was including higher in the case of *Calothrix* and *Anabaena*, with more than 70 %d.wt. of carbohydrates. In terms of proteins, the strain showing a higher protein content was *Spirulina*, up to 60%d.wt., whereas *Anabaena* and *Calothrix* shows the lowest contents, lower than 20 %d.wt., in spite that all of them are cyanobacteria. Similar biochemical composition to that here showed has been previously described for *Chlorella vulgaris* ([59]), *Scenedesmus* ([60]), and *Neochloris* ([61]). The different biochemical composition of the produced biomass indicate that each one of them could be used for different purposes as biofuels, biofertilizers, animal feed, etc. [62,63] However, the biomass value varies in the diverse applications so, to achieve a reliable process, it is necessary to identify a target market where the biomass value will be higher than its production cost.[19]

As stated in the introduction, the choosing of the final strain to be used at large scale also depends on the value of the produced biomass and the economic yield of the process

(**Fig. 4**). To determine these values a standard value of proteins (1 €/kg), lipids (0.6 €/kg) and carbohydrates (0.3 €/kg) has been considered, these values corresponding to the approximate price of these commodities. All the microalgae/cyanobacteria biomasses produced have an equivalent value, ranging from maximal value of 0.7 €/kg of *Spirulina*, to the minimum value of 0.4 €/kg of *Anabaena* (**Fig. 4A**). It is noticeable the high value of *Neochloris* because this strain have been widely reported as interesting for biodiesel production,[56] in addition to *Nostoc* which has been reported as a robust strain suitable to be produced at large scale.[64] However, *Spirulina* and *Nostoc* were some of the less productive strains. Multiplying the value of the biomass by the biomass productivity, i.e., the economic yield, is a more interesting criterion. The results that *Scenedesmus* is the most interesting strain in this respect, its economic yield being of 0.87 €/m^3·day (**Fig. 4B**).

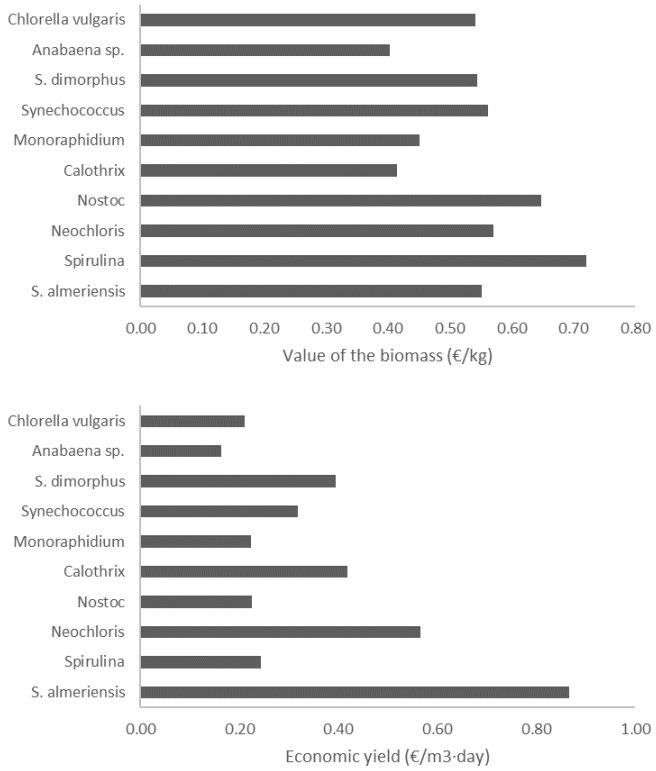

Figure 4. Value of the biomass and economic yield of the system of different strains tested at laboratory conditions.

3.4 Biomass production and photosynthetic efficiency at outdoor conditions

Once the optimal strain has been selected, it was tested in real outdoor conditions, using a 100 m^2 pilot scale raceway reactor operated in continuous mode at 0.2 day^{-1} during six months from January to June at Almeria (Spain). On this time the solar radiation changes from 11 to 30 $MJ/m^2 \cdot day$ whereas the mean daily temperature ranged from 12ºC in winter time to 25ºC in summer time. In spite of large variations of solar radiation and temperature, not only along the days but also in each solar cycle, the cultures of *Scenedesmus* perform adequately, no large contamination problems existing and the culture being stable for long time (**Fig. 5**). Data shows as the biomass productivity increases from 10 to 30 $g/m^2 \cdot day$ from January to June mainly by the increase on solar radiation availability. On this time the photosynthetic efficiency did not change too much, a really high mean value of 2.0% being measured. These values confirm the adequacy of the selected strain to be used in large scale CO_2 capture processes.

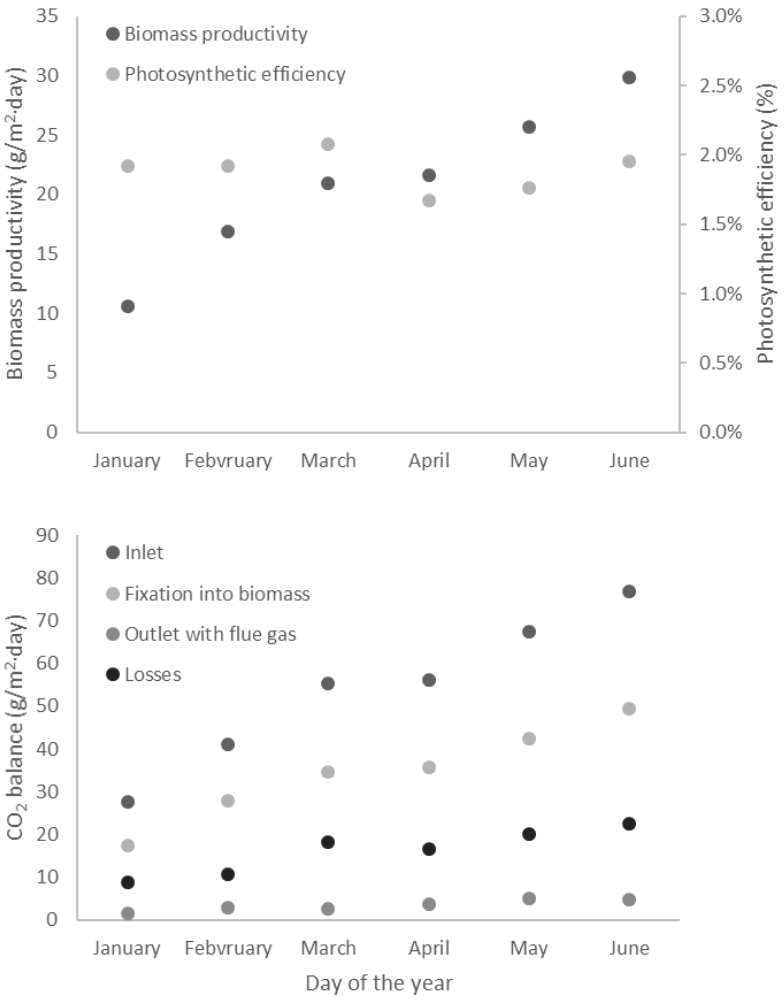

Figure 5. Variation of biomass productivity and photosynthetic efficiency **(A),** in addition to CO_2 inlet and outlet streams, of outdoor continuous cultures of Scenedesmus almeriensis in a 100 m^2 pilot scale raceway reactor located in Almeria (Spain).

To determine the real CO_2 capture capacity, the mass flow of CO_2 entering to the reactor was measured, in addition to the net amount of CO_2 fixed into the biomass, and the CO_2 losses with the flue gases exhausting the reactor. The difference between the CO_2 inlet and the CO_2 outlet with the biomass and the flue gases was calculated as overall CO_2 losses. The results indicate that the CO_2 demand of the system increases when increasing the biomass productivity, due to the control system used to maintain the pH at its optimal value (Fig. 5b). The total CO_2 demand ranged from 27.6 to 76.7 g/m^2·day. This CO_2 was mainly consumed by the biomass, their values ranging from 17.5 to 49.3 g/m^2·day. The larger amount of CO_2 supplied with respect to the net amount fixed into the biomass was

due to the efficiency of the CO_2 supply system. Thus, CO_2 losses by non-absorption of CO_2 contained into the flue gases injected ranges from 1.4 to 4.8 g/m^2·day. These values are really minor when comparing with total CO_2 supplied, indicating the adequate performance of the CO_2 gas supply system. However, still a large fraction of CO_2 was lost, ranging from 8.7 to 22.6 g/m^2·day. These losses can be due to decarbonisation into the entire raceway reactor or carbon outlet with the outlet culture broth when harvesting. Anyway, the total amount of CO_2 demanded by the system was **54 g/m^2·day**, equivalent to 197 t/ha·year. This means that the CO_2 demand to biomass productivity ratio is 2.58, instead of the 1.83 value theoretically obtained if considering the basic equation of photosynthesis. This is an important fact considering CO_2 emissions at ground level or the increase of inorganic carbon concentration in the exhausted water for its final disposal. On average, the CO_2 fixation into the biomass represent 64.0% of the total CO_2 inlet, whereas CO_2 losses with the exhaust gas represent 9.6% of the total CO_2 inlet, then the remaining CO_2 losses representing up to 26.4% of total CO_2 inlet. Although raceway reactors are the most suitable for CO_2 capture-related processes other technologies has been previously studied. By comparing the performance of *Anabaena* cultures carried out in raceway, tubular photobioreactors and flat panels, the optimal value of 35 g/m^2·day was achieved in flat panels reactors.[65] However, the scale-up of this technology is still a major issue in microalgae biotechnology field.

4. DISCUSSION

As mentioned in the introduction the purpose of this work is to analyze and compare the capability of CO_2 capture by a physicochemical means (adsorption in porous media) and by biological means (biomass production by microalgae). In this respect, not only the rate of CO_2 capture is of importance, but also the energy requirements of the process and the valorization of the final product.

As regards the former, the separation performance of the proposed dual-PSA process with the best performing zeolite MFI provides a figure of 8 kg m^{-3} bed h^{-1}, which is substantially higher that previously reported data by microalgae (0.04-0.25 kg m^{-3} broth h^{-1})[66] and the data presented in this work: 0.00225 kg m^{-2} h^{-1}. On the other hand the energy requirement is lower than the one of amine scrubbing processes (0.37 kWh/kg$CO_{2captured}$ =

1.3 MJ/kg$CO_{2captured}$).[67] As regards the economic aspect, the obtained product (high purity CO_2) can be used in many applications, such as the obtention of carbon monoxide, methane or methanol.

With respect to the biological alternative, it must borne in mind that the CO_2 supply system must be accurately designed to avoid reemission of CO_2 to the atmosphere. Carbon dioxide can be supplied to microalgae cultures by (a) continuous bubbling or (b) on-demand injection. With continuous bubbling of flue gases, the medium becomes acidic and maximum CO_2 use efficiencies of only 8.1 % [68] and 4.2 % [69] have been reported. With on-demand injection of flue gases, a maximum CO_2 use efficiency of 32.8 % in open photobioreactors [70] and 50 % in closed photobioreactors[71] have been determined. In both strategies, the consumption of CO_2 is a function of the design and the operation of the carbonation unit, and finally, of the mass transfer phenomena into the culture. In a different strategy the CO_2 can be provided dissolved into the culture medium by passing it by a previous carbonation unit, up to 2.0 g/L of total inorganic carbon being dissolved into the culture medium suitable to be consumed by *Anabaena* [72]. Recently the CO_2 capture efficiency in raceway reactors has been re-designed by including a sump into the reactor, and optimizing its design and gas/liquid flow rates. It was demonstrated that under optimal conditions de CO_2 transfer efficiency was up to 98% [73].

On top of all these considerations, the energy consumption and cost of the biological process must also be analysed. In the case of energy, the major energy inlet on raceway reactors is the power required by the paddlewheel. To minimize the energy consumption, raceway reactors are build following some key rules, as a length to wide ratio of 10, using softer as possible materials, reducing the liquid velocity up to 0.2 m/s, and minimizing the presence of bends and other structural parts that disturb the flow along the channels [74]. Recently the design of this type of reactors has been reviewed to minimize its energy consumption. In this respect a new Low Energy Algae Reactor (LEAR Patent EP2875724A1) has been patented. Thus, energy consumption in raceway reactors can be reduced from 20 to 1 W/m^3,[21] or including below 1 W/m^3 if using LEAR system. During the operation of the 100 m^2 pilot scale raceway reactor the measured energy consumption was 2 W/m^3, thus it being equivalent to 0.48 MJ/kg of CO_2 captured, which is substantially

lower than the chemical (amines scrubbing) and physicochemical (zeolite adsorption) procedures.

In **Fig. 6** the influence of biomass productivity and specific energy consumption on the raceway reactor into the specific energy consumption per kg of CO_2 captured is analized. It is confirmed that microalgae based processes have lower energy consumption that amines-based processes only when specific energy consumption of the reactor are lower than 20 W/m^3 and at biomass productivities are higher than 25 $g/m^2 \cdot day$. When comparing with zeolites-based processes the microalgae have lower energy consumption only when operating at specific energy consumption in the raceway reactor lower than 2 W/m^3 and biomass productivities higher than 15 $g/m^2 \cdot day$. Anyway, these figures show that the microalgae-based processes for CO_2 capture are in the same range of energy consumption than low energy demanding technologies as PSA with zeolites. In terms of cost, the biomass production cost in this type of raceway reactors can be reduced till 2.1 €/kg when using flue gases and minimum manpower (0.1 men/ha), it being equivalent to a CO_2 capture cost of 0.8 €/kg [75]. This production cost is much higher than conventional price of industrial pure CO_2, ranging from 0.1-0.2 €/kg. However, the price of microalgae biomass is much higher than of pure CO_2, minimum values of 5 €/kg being reported [76]. Considering this price for the biomass, the value of CO_2 contained into the biomass is 1.9 €/kg, much higher than estimated CO_2 capture cost of 0.8 €/kg. Thus, to achieve a suitable commercial process for CO_2 capture, it is necessary to produce valuable biomass otherwise the production cost will be higher than the CO_2 emission taxes [19].

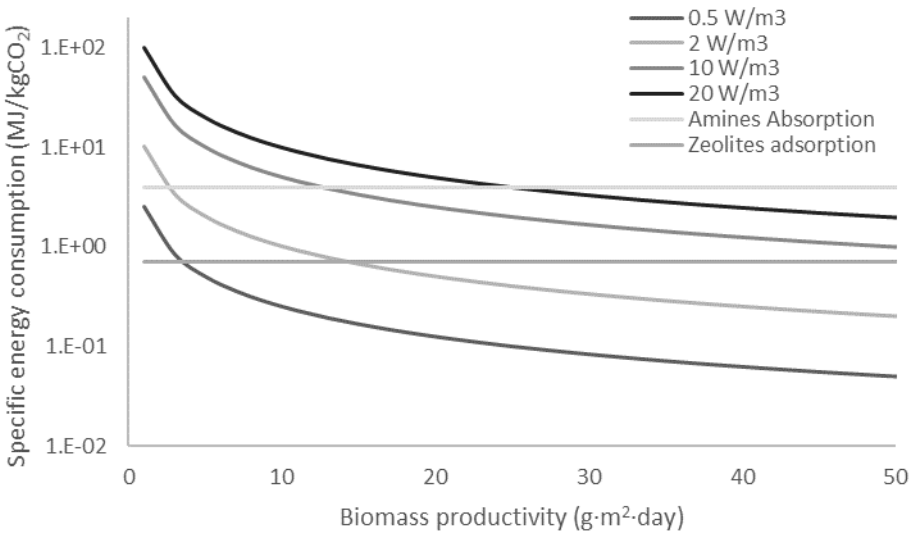

Figure 6. Variation of energy consumption of microalgae based processes as a function of biomass productivity and specific energy consumption of the reactor.

5. CONCLUSIONS

The alternative capabilities of a physicochemical (adsorption in porous media) and a biological process (biomass production by microalgae) to capture CO_2 from flue gases has been analysed, assessed and compared.

In connection to the physicochemical alternative, GEMC simulations and adsorption experiments demonstrate that commercial zeolite MFI is the best candidate to capture this gas due to the morphology and crystalline structure of this material. Numerical simulation of a dual PSA cycle suitable for industrial implementation confirms this finding and provide an estimated value for CO_2 capture of 8 kg m^{-3} bed h^{-1} and an energy compsuption of 0.987 MJ/Kg of captured CO_2.

In connection to the biological alternative, it is demonstrated that microalgae-based processes for capturing CO_2 from flue gases can be performed, being reliable at real outdoor operation conditions for more than six months. The key factors determining the reliability of the process are the selection of adequate strains and technologies. From the up to ten microalgae/cyanobacteria strains evaluated, the fast growing and robust *Scenedesmus almeriensis* was the more productive, up to 0.06 kg m^{-3} broth h^{-1}. The production of this

strain in a 100 m^2 pilot scale raceway reactor at real outdoor conditions was demonstrated, allowing to capture up to 54 $gCO_2/m^2 \cdot day$ in average from January to June. The strategy of on-demand supply of CO_2 and optimal mass transfer capacity into the reactor allows to capture up to 2.58 $kgCO_2$ per kg of produced biomass, only 9.6% of the supplied CO_2 being lost to the atmosphere. Energy consumption of the process was estimated at 0.48 $MJ/kgCO_2$, the unitary cost being 0.8 €/kg of CO_2. The energy consumption is lower than the physicochemical process, but the cost is much high than regular price of pure CO_2. However, value of the microalgae biomass is much higher thus it being concluded that captured CO_2 have a value equivalent to 1.9 €/kg. These figures provide a realistic scenario about the potential application of microalgae to CO_2 capture related processes.

Although the major bottleneck of microalgae-based processes is the necessity of high sunlight and land availability, this technology can be an alternative for diffuse CO_2 emission from small industries and farms, among others. Physicochemical processes do not depend on ambient conditions and land availability but rely on a suitable use and management of the resulting stream of pure CO_2 obtained.

ACKNOWLEDGEMENTS

This study was carried out with the financial support of Junta de Andalucía, grant FQM 1851 and the company, SETEC. We are grateful for the practical assistance kindly given by the staff of the Las Palmerillas Experimental Station, part of the Cajamar Foundation.

6. REFERENCES

1 Anonymous, Paris Agreement, https://ec.europa.eu/clima/policies/international/negotiations/paris_en, (accessed 16 March 2019).

2 M. Collins, R. Knutti, J. Arblaster, J.-L. Dufresne, T. Fichefet, P. Friedlingstein, X. Gao, W. J. Gutowski, T. Johns, G. Krinner, M. Shongwe, C. Tebaldi, A. J. Weaver and M. Wehner, *Clim. Change 2013 Phys. Sci. Basis Contrib. Work. Group Fifth Assess. Rep. Intergov. Panel Clim. Change*, 2013, 1029–1136.

3 E. Herzog, H., Drake E., Adams, *EM Featrure*, 1997, 22–24.
4 O. US EPA, Sources of Greenhouse Gas Emissions, https://www.epa.gov/ghgemissions/sources-greenhouse-gas-emissions, (accessed 16 March 2019).
5 C.-H. Yu, C.-H. Huang and C.-S. Tan, *Aerosol Air Qual. Res.*, 2012, **12**, 745–769.
6 G. T. Rochelle, *Science*, 2009, **325**, 1652–1654.
7 J.-L. Li and B.-H. Chen, *Sep. Purif. Technol.*, 2005, **41**, 109–122.
8 M. J. Tuinier, H. P. Hamers and M. van Sint Annaland, *Int. J. Greenh. Gas Control*, 2011, **5**, 1559–1565.
9 Global CCS Institute, *The global status of ccs: 2011*, 2011.
10 M. T. Ho, G. W. Allinson and D. E. Wiley, *Ind. Eng. Chem. Res.*, 2008, **47**, 4883–4890.
11 Q. Wang, J. Luo, Z. Zhong and A. Borgna, *Energy Environ. Sci.*, 2010, **4**, 42–55.
12 Z. Zhao, Z. Li and Y. S. Lin, *Ind. Eng. Chem. Res.*, 2009, **48**, 10015–10020.
13 J. M. Vicent-Luna, J. J. Gutiérrez-Sevillano, J. A. Anta and S. Calero, *J. Phys. Chem. C*, 2013, **117**, 20762–20768.
14 E. Hughes and J. R. Benemann, *Energy Convers. Manag.*, 1997, **38**, S467–S473.
15 U. B. Singh and A. S. Ahluwalia, *Mitig. Adapt. Strateg. Glob. Change*, 2013, **18**, 73–95.
16 S.-H. Ho, C.-Y. Chen, D.-J. Lee and J.-S. Chang, *Biotechnol. Adv.*, 2011, **29**, 189–198.
17 J. C. M. Pires, M. C. Alvim-Ferraz, F. G. Martins and M. Simões, *Renew. Sustain. Energy Rev.*, 2012, **16**, 3043–3053.
18 W. Zhou, J. Wang, P. Chen, C. Ji, Q. Kang, B. Lu, K. Li, J. Liu and R. Ruan, *Renew. Sustain. Energy Rev.*, 2017, **76**, 1163–1175.
19 F. G. Acien, C. V. González-López, J. M. Fernández-Sevilla and E. Molina-Grima, *Appl. Microbiol. Biotechnol.*, 2012, **96**, 577–586.
20 M. R. Tredici, *Biofuels*, 2010, **1**, 143–162.
21 J. L. Mendoza, M. R. Granados, I. de Godos, F. G. Acién, E. Molina, C. Banks and S. Heaven, *Biomass Bioenergy*, 2013, **54**, 267–275.
22 J. L. Mendoza, M. R. Granados, I. de Godos, F. G. Acién, E. Molina, S. Heaven and C. J. Banks, *Bioresour. Technol.*, 2013, **137**, 188–195.
23 R. K. Desai, M. Streefland, R. H. Wijffels and M. H. M. Eppink, *Green Chem.*, , DOI:10.1039/c3gc42631a.
24 S. De Caralt, M. J. Uriz and R. H. Wijffels, *J. Mar. Biol. Assoc. U. K.*, , DOI:10.1017/S0025315407056846.
25 F. G. Acién, C. Gómez-Serrano, M. M. . Morales-Amaral, J. M. Fernández-Sevilla and E. Molina-Grima, *Appl. Microbiol. Biotechnol.*, 2016, **100**, 9013–9022.
26 S. Venkata Mohan, M. V. Rohit, P. Chiranjeevi, R. Chandra and B. Navaneeth, *Bioresour. Technol.*, , DOI:10.1016/j.biortech.2014.10.056.
27 D. Frenkel and B. Smit, *Understanding Molecular Simulations: From Algorithms to Applications*, C. Academic Press, San Diego, CA, second edi., 2002.
28 D. Dubbeldam, S. Calero, D. E. Ellis and R. Q. Snurr, *Mol. Simul.*, 2015, **42**, 81–101.
29 D. Dubbeldam, A. Torres-Knoop and K. S. Walton, *Mol. Simul.*, 2013, **39**, 1253–1292.
30 I. Matito-Martos, A. Martin-Calvo, J. J. Gutiérrez-Sevillano, M. Haranczyk, M. Doblare, J. B. Parra, C. O. Ania and S. Calero, *Phys Chem Chem Phys*, 2014, **16**, 19884--19893.
31 E. Garcia-Perez, J. B. Parra, C. O. Ania, A. Garcia-Sanchez, J. M. Van Baten, R. Krishna, D. Dubbeldam and S. Calero, *Adsorpt.-J. Int. Adsorpt. Soc.*, 2007, **13**, 469–476.
32 A. Garcia-Sanchez, C. O. Ania, J. B. Parra, D. Dubbeldam, T. J. H. Vlugt, R. Krishna and S. Calero, *J. Phys. Chem. C*, 2009, **113**, 8814–8820.

33 A. Martin-Calvo, E. Garcia-Perez, A. Garcia-Sanchez, R. Bueno-Perez, S. Hamad and S. Calero, *Phys. Chem. Chem. Phys.*, 2011, **13**, 11165–11174.
34 S. W. Rick, *J. Chem. Phys.*, 2004, **120**, 6085–6093.
35 T. J. H. Vlugt and M. Schenk, *J. Phys. Chem. B*, 2002, **106**, 12757–12763.
36 S. Calero, D. Dubbeldam, R. Krishna, B. Smit, T. J. H. Vlugt, J. F. M. Denayer, J. A. Martens and T. L. M. Maesen, *J. Am. Chem. Soc.*, 2004, **126**, 11377–11386.
37 R. Krishna and J. M. van Baten, *Langmuir*, 2010, **26**, 2975–2978.
38 I. Matito-Martos, J. Álvarez-Ossorio, J. J. Gutiérrez-Sevillano, M. Doblaré, a. Martin-Calvo and S. Calero, *Phys Chem Chem Phys*, 2015, **17**, 18121–18130.
39 I. Matito-Martos, A. Rahbari, A. Martin-Calvo, D. Dubbeldam, T. J. H. Vlugt and S. Calero, *Phys. Chem. Chem. Phys.*, 2018, **20**, 4189–4199.
40 S. Effendy, C. Xu and S. Farooq, *Ind. Eng. Chem. Res.*, 2017, **56**, 5417–5431.
41 J. Park, R. P. Lively and D. S. Sholl, *J Mater Chem A*, 2017, **5**, 12258–12265.
42 R. R. Vemula and S. Sircar, *AIChE J.*, **63**, 4066–4078.
43 A. L. Myers and J. M. Prausnitz, *AIChE J.*, 1965, **11**, 121–127.
44 I. Langmuir, *J. Am. Chem. Soc.*, 1918, **40**, 1361–1403.
45 C. A. Grande and R. Blom, *Energy Procedia*, 2012, **26**, 2–14.
46 M. Barceló-Villalobos, J. L. Guzmán Sánchez, I. Martín Cara, J. A. Sánchez Molina and F. G. Acién Fernández, *Algal Res.*, 2018, **35**, 91–97.
47 J. M. Fernández-Sevilla, E. Molina-Grima, F. García-Camacho, F. G. Acién and J. A. Sánchez-Pérez, *Appl. Microbiol. Biotechnol.*, 1998, **50**, 199–205.
48 E. Molina Grima, F. García Camacho, J. A. Sánchez Pérez, F. G. Acién, J. M. M. Fernández Sevilla, J. A. Sánchez Pérez, F. G. Acién Fernández and J. M. M. Fernández Sevilla, *J. Appl. Phycol.*, 1996, **8**, 529–534.
49 G. Kochert, *Handb. Phycol. Methods*, 1978, **2**, 95–97.
50 C. V. González López, M. del C. Cerón García, F. G. Acién Fernández, C. Segovia Bustos, Y. Chisti and J. M. Fernández Sevilla, *Bioresour. Technol.*, 2010, **101**, 7587–7591.
51 S. Sircar, *Ind. Eng. Chem. Res.*, 2006, **45**, 5435–5448.
52 J.-R. Li, R. J. Kuppler and H.-C. Zhou, *Chem. Soc. Rev.*, 2009, **38**, 1477–1504.
53 M. M. Morales-Amaral, C. Gómez-Serrano, F. G. Acién, J. M. Fernández-Sevilla and E. Molina-Grima, *Algal Res.*, 2015, **9**, 297–305.
54 T. Duarte-Santos, J. L. Mendoza-Martín, F. G. Acién Fernández, E. Molina, J. A. Vieira-Costa and S. Heaven, *Bioresour. Technol.*, 2016, **212**, 72–81.
55 J. F. S. Fernández, C. V. González-López, F. G. A. Fernández, J. M. F. Sevilla and E. M. Grima, *Appl. Microbiol. Biotechnol.*, , DOI:10.1007/s00253-011-3683-7.
56 J. Pruvost, G. Van Vooren, G. Cogne and J. Legrand, *Bioresour. Technol.*, 2009, **100**, 5988–5995.
57 L. Gouveia, A. E. Marques, T. L. Da Silva and A. Reis, *J. Ind. Microbiol. Biotechnol.*, 2009, **36**, 821–826.
58 C. Gómez-Serrano, M. M. Morales-Amaral, F. G. Acién, R. Escudero, J. M. Fernández-Sevilla and E. Molina-Grima, *Appl. Microbiol. Biotechnol.*, 2015, **99**, 6931–6944.
59 C. D. Calixto, J. K. da Silva Santana, E. B. de Lira, P. G. P. Sassi, R. Rosenhaim, C. F. da Costa Sassi, M. M. da Conceição and R. Sassi, *Bioresour. Technol.*, 2016, **221**, 438–446.
60 L. Yao, J. A. Gerde, S. L. Lee, T. Wang and K. A. Harrata, *J. Agric. Food Chem.*, 2015, **63**, 1773–1787.

61 C. A. Popovich, C. Damiani, D. Constenla, A. María Martínez, H. Freije, M. Giovanardi, S. Pancaldi and P. I. Leonardi, , DOI:10.1016/j.biortech.2012.02.121.
62 Q. Hu, M. Sommerfeld, E. Jarvis, M. Ghirardi, M. Posewitz, M. Seibert and A. Darzins, 2008, 54, 621–639.
63 A.-M. Lakaniemi, O. H. Tuovinen and J. A. Puhakka, *Bioresour. Technol.*, 2013, **135**, 222–31.
64 R. Piccardi, A. Frosini, M. R. Tredici and M. C. Margheri, *J. Appl. Phycol.*, 2000, **12**, 543–547.
65 M. E. Clares, J. Moreno, M. G. Guerrero and M. García-González, *J. Biotechnol.*, 2014, **187**, 51–55.
66 A. Ghorbani, H. R. Rahimpour, Y. Ghasemi, S. Zoughi and M. R. Rahimpour, *Renew. Sustain. Energy Rev.*, 2014, **35**, 73–100.
67 G. T. Rochelle, *Science*, 2009, **325**, 1652–1654.
68 Z. Cheng-wu, O. Zmora, R. Kopel and A. Richmond, *Aquaculture*, 2001, **195**, 35–49.
69 Q. Hu, N. Kurano, M. Kawachi, I. Iwasaki and S. Miyachi, *Appl.Microbiol.Biotechnol.*, 1998, **49**, 655–662.
70 J. Doucha, F. Straka, K. Lívanský and K. Lívanský, *J. Appl. Phycol.*, 2005, **17**, 403–412.
71 F. Camacho Rubio, F. G. Acién Fernández, J. A. Sánchez Pérez, F. García Camacho and E. Molina Grima, *Biotechnol. Bioeng.*, 1999, **62**, 71–86.
72 C. V. V González-López, F. G. A. Fernández, J. M. M. Fernández-Sevilla, J. F. S. Fernández, E. M. Grima, C. V. Gonz??lez-L??pez, F. G. Aci??n Fern??ndez, J. M. Fern??ndez-Sevilla, J. F. S??nchez Fern??ndez, E. Molina Grima, C. V. V González-López, F. G. Acién Fernández, J. M. M. Fernández-Sevilla, J. F. Sánchez Fernández, E. Molina Grima, F. G. A. Fernández, J. M. M. Fernández-Sevilla, J. F. S. Fernández and E. M. Grima, *Biotechnol. Bioeng.*, 2012, **109**, 1637–1650.
73 I. de Godos, J. L. Mendoza, F. G. Acién, E. Molina, C. J. Banks, S. Heaven and F. Rogalla, *Bioresour. Technol.*, 2014, **153**, 307–314.
74 J. C. Weissman and R. P. Goebel, *Design and analysis of microalgal open pond systems for the purpose of producing fuels: A subcontract report*, 1987.
75 F. G. Acién, J. M. Fernández, J. J. Magán and E. Molina, *Biotechnol. Adv.*, 2012, **30**, 1344–1353.
76 P. Spolaore, C. Joannis-Cassan, E. Duran and A. Isambert, *J. Biosci. Bioeng.*, 2006, **101**, 87–96.

Potential of CO_2 capture from flue gases by physicochemical and biological methods: a comparative study – Supporting Information

Ismael Matito-Martos[a,¶], Claudia Sepulveda[b,¶,*], Cintia Gómez[c], Gabriel Acién[c], , Julio Perez-Carbajo[a], J. A. Delgado [d], V. I. Águeda[d], Conchi Ania[e], J. B. Parra[f], S. Calero[a] and J. A. Anta[a]*

¶[x]these two authors contributed equally to this work.

[a]*Department of Physical, Chemical and Natural Systems, University Pablo de Olavide, Sevilla 41013, Spain*
[b] *Bio-innovation Centre*, Antofagasta Institute, University of Antofagasta, Chile

[c]*Department of Chemical Engineering*, University of Almería, 04120 Almería, Spain

[d]*Department of Chemical Engineering, Universidad Complutense de Madrid, 28040, Madrid, Spain*

[e]*CEMTHI (CNRS UPR 3079) Université d'Orléans, 45071, Orléans, France.*

[f]*Instituto Nacional del Carbón, INCAR, CSIC, P.O. 73, 33080 Oviedo, Spain.*

Corresponding authors*: Claudia Sepúlveda (Claudia.sepulveda@uantof.cl), Juan A. anta (anta@upo.es)

Section A. Details of interaction potentials for CO_2, N_2, O_2 and H_2O

Atomic interactions were taken into account using electrostatic (Coulomb) and Van de Waals (Lennard-Jones) forces. For CO_2, each interaction site corresponds to an atom center, with both partial charge and Lennard-Jones parameters assigned.[1] Central dummy pseudo-atoms (D), with partial charges but without mass or Lennard-Jones parameters, are defined for O_2 and N_2 to reproduce their first non-zero electrostatic moment.[2] The water molecule is described by the TIP5P/Ew model.[3] This model has already been proved as suitable for studying adsorption of water in zeolites.[4,5] This molecule is modeled by the O atom, the two H atoms and two extra dummy atoms (M) with tetrahedral site distribution, with the O at the center. There is only a single dispersive center at the O, and point charges

are located at the H and M sites, the latter accounting for the negative partial charge of the oxygen atom.[3] Adsorbate-adsorbate cross van der Waals interactions are taken into account by Lorentz–Berthelot mixing rules.[6] In the case of zeolites, every Si atom is surrounded by four O atoms, and so the latter dominate the dispersive forces. The adsorbate-framework interactions are defined by those of the framework O atoms with the atoms of the adsorbed molecules. Since zeolites not always obey the Lorentz–Berthelot mixing rules for the adsorbate–framework interactions, Lennard-Jones parameters need to be independently adjusted.[1,7] To reproduce the interaction of CO_2, N_2 and O_2, and water with the zeolite, in this work we used parameters from Garcia-Sanchez *et al.*,[1] Martin-Calvo *et al.*,[8] and Castillo *et al.*,[9] respectively. The set of charges for the framework atoms was also taken from Garcia-Sanchez *et al.*[1] All Lennard-Jones parameters and partial charges used in this work are collected in Table S1.

Table S1. Lennard-Jones parameters and partial charges of the adsorbates and the adsorbents

Atom 1	Atom 2	ε/k_B (K)	σ (Å)	Charge (e^-)
Adsorbed Molecules				
$C(CO_2)$	$C(CO_2)$	29.933	2.745	0.651
$O(CO_2)$	$O(CO_2)$	85.671	3.017	-0.326
$O(O_2)$	$N(O_2)$	53.023	3.045	-0.112
$D(O_2)$	$D(O_2)$	-	-	0.224
$N(N_2)$	$N(N_2)$	38.298	3.306	-0.405
$D(N_2)$	$D(N_2)$	-	-	0.810
$O(H_2O)$	$O(H_2O)$	89.516	3.097	-
$H(H_2O)$	$H(H_2O)$	-	-	0.241
$M(H_2O)$	$M(H_2O)$	-	-	-0.241
Zeolite				
O(zeo)	O(zeo)	-	-	-0.393
Si(zeo)	Si(zeo)	-	-	0.786
Adsorbed Molecules - Zeolite				
$C(CO_2)$	O(zeo)	37.595	3.511	-
$O(CO_2)$	O(zeo)	78.98	3.237	-
$O(O_2)$	O(zeo)	60.189	3.129	-
$D(O_2)$	O(zeo)	-	-	-
$N(N_2)$	O(zeo)	60.580	3.261	-
$D(N_2)$	O(zeo)	-	-	-
$O(H_2O)$	O(zeo)	13.710	3.377	-
$H(H_2O)$	O(zeo)	-	-	-
$M(H_2O)$	O(zeo)	-	-	-

Section B. Morphological and structural description of the zeolites

BEA, MOR, FER, and MFI are zeolites with a structure consisting of interconnected channels with different directionality. Crystallographic positions of zeolite BEA were taken from Newsam *et al.*[10] This structure has a 3-dimensional pore structure, with straight 12 membered-ring (MR) channels parallel to *x*- and *y*-axes with pore limiting diameters around 6-7 Å*;* and zig-zag 12MR pore path along the *z*-direction with a 5.6 Å limiting diameter. Crystallographic positions of the atoms of zeolite MOR were taken from the work of Gramlich.[11] This zeolite is formed by parallel channels in the *z*-axis, with 12MR windows; and additional adsorption sites in the *y*-axis, so called side pockets. Channels and pockets can be observed in the peaks in the Pore Size Distribution (PSD) in **Fig. S1** at ca. 6 and 4.2 Å respectively. Pockets are accessible from the main channels only for small molecules.[12] FER shows a 2-dimensional intersected system of channels of 4.7 Å (10-membered rings along *z*-axis) and 3.4 Å (8-membered rings along *y*-axis) limiting diameters.[13] 10-members rings also configure main channels of MFI zeolite (*x*-axis), which are intersected by zig-zag secondary channels leading to a 3-dimensional system with limiting diameters around 4.5-4.7 Å.[14] The two last zeolites under study, ITQ-29 and FAU, have cubic cells of 11.87 and 24.26 Å, respectively. In this work we used crystallographic positions reported by Corma *et al.* (ITQ-29),[15] and Hriljac *et al.* (FAU).[16] Both zeolites show two types of interconnected cages (as can be seen from the two mains picks in the PSD in **Fig S1**). In FAU, the biggest cages (α-cages) are accessible through 12MR windows, with a limiting diameter of around 7.1 Å; while in ITQ-29, LTA-cages are accessible through an 8MR window, resulting on a lower limiting diameter (4.1 Å). For both structures, β-cages or sodalites are not accessible for most molecules due to the narrow windows that connect them with bigger cages (4- and 6-meber rings, respectively).

Table S2 Structural and topological properties of the zeolites under study.

Zeolite	Pore Volume (cm3g)	Surface Area (m^2/g)	Density (kg/m3)	Channel System	Channel Diameter	Channel Diameter	Channel Diameter	Ring sizes
BEA	0.277	984.93	1508.521	3D	5.95	5.95	5.95	12 6 5 4
FAU	0.332	1020.88	1342.047	3D -Cages	7.35	7.35	7.35	12 6 4
FER	0.066	235.07	1837.870	2D (1D)	4.69	3.4	-	10 8 6 5
ITQ-29	0.286	849.28	1432.806	3D-Cages	4.21	4.21	4.21	8 6 4
MOR	0.150	477.92	1711.056	1D	6.45	-	-	12 8 5 4
MFI	0.164	547.67	1796.342	3D	4.7	4.46	4.46	10 6 5 4

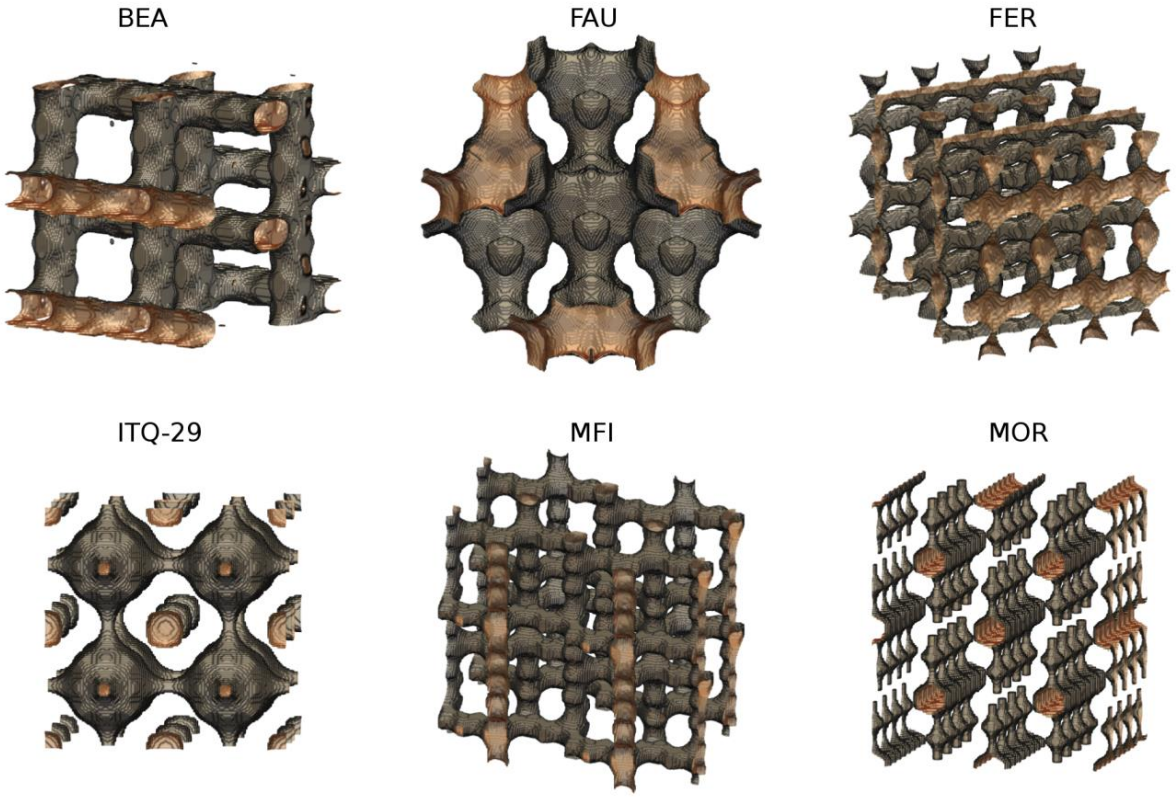

Figure S1. Energy grid surface of BEA, FAU, and FER zeolites (top) and ITQ-29, MFI and MOR zeolites (down). The accessible surface is colored in brown and the inaccessible surface in grey.

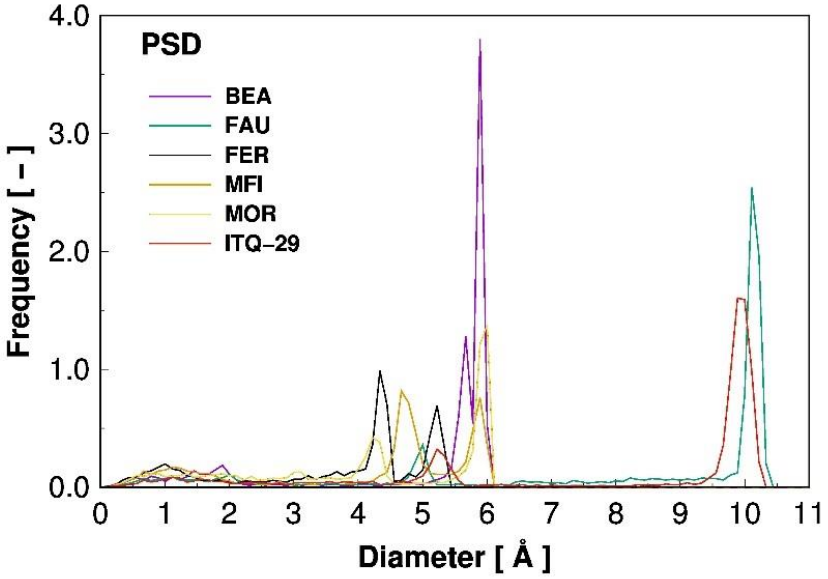

Fig. S2. Pore-size distributions of the zeolites under study.

Section C. Details of PSA simulations

PSA simulations have been carried out with PSASIM software.[17] Parameters of the simulation are collected in **Table S3**. PSA numerical simulations were performed using the cycle shown in **Fig. S3** (adiabatic conditions) to discriminate between the separation performance of the different zeolites. Subsequently, a dual cycle (**Figure S4**) was used to improve the yield of CO_2 zeolite for the MFI zeolite only.

The multicomponent adsorption isotherms for the PSA simulations were obtained by applying the IAST method to the pure component adsorption isotherms, previously obtained by GCMC simulations. Isotherms were fitted with the Langmuir model. A comparison between the pure component adsorption isotherms and the fitted ones is shown in **Fig. S5**. The fitted Langmuir parameters are shown in **Table S4**. A comparison between the multicomponent equilibrium data calculated with both methods is shown in **Table S5**. The introduction a correction factor for the adsorbed concentration of CO_2 calculated from IAST method ranging between 0.93 and 1.02 was necessary to accurately predict multicomponent equilibrium data obtained from molecular simulation. The good agreement between the obtained results after applying the correction can be observed in the Table S5.

Table S3. Model parameters and operating conditions for PSA simulations.

Feed gas mixture	$N_2/CO_2/O_2/H_2O$
Feed composition, %v/v	75/10/11/3.2
Feed temperature, K	298
P_H, P_L, bar	1,0.1
Feed gas velocity, m s^{-1}	0.2
Purge superficial velocity, m s^{-1}	0.15
Bed length, m	1
Bed radius, m	0.1
Bed porosity	0.4
Intraparticle porosity	0.3
[a]Particle density, kg m^{-3}	crystal density*(1-intraparticle porosity)
Particle radius, m	$0.7 \cdot 10^{-3}$

Adsorbent heat capacity, J kg^{-1} K^{-1}	1000
[b]Molecular diffusivity, m^2 s^{-1}	$1 \cdot 10^{-5}$
Tortuosity	3
[b]k_g, J s^{-1} m^{-1} K^{-1}	0.06
[b]μ, Pa s	$1.8 \cdot 10^{-5}$

[a]The following crystal densities have been employed (kg m^{-3}). BEA: 1508; FAU: 1342; FER: 1838; ITQ-29: 1433; MFI: 1796; MOR: 1711.
[b]Calculated with AspenPlus program

Table S4. Fitted Langmuir parameters in the studied structures at 298 K

Gas/Structure	K_H, **mol kg^{-1} Pa^{-1}**	b, **Pa^{-1}**
N_2/BEA	$1.693 \cdot 10^{-6}$	$4.960 \cdot 10^{-7}$
CO_2/BEA	$1.946 \cdot 10^{-5}$	$3.679 \cdot 10^{-6}$
O_2/BEA	$1.324 \cdot 10^{-6}$	$2.873 \cdot 10^{-7}$
H_2O/BEA	$1.096 \cdot 10^{-7}$	$2.193 \cdot 10^{-8}$
N_2/FAU	$9.132 \cdot 10^{-7}$	$1.338 \cdot 10^{-7}$
CO_2/FAU	$4.844 \cdot 10^{-6}$	$-1.006 \cdot 10^{-6}$
O_2/FAU	$7.853 \cdot 10^{-7}$	$5.259 \cdot 10^{-8}$
H_2O/FAU	$1.565 \cdot 10^{-7}$	$1.565 \cdot 10^{-12}$
N_2/FER	$1.280 \cdot 10^{-6}$	$1.004 \cdot 10^{-6}$
CO_2/FER	$1.775 \cdot 10^{-5}$	$1.559 \cdot 10^{-5}$
O_2/FER	$1.088 \cdot 10^{-6}$	$7.494 \cdot 10^{-7}$
H_2O/FER	$3.972 \cdot 10^{-8}$	$3.972 \cdot 10^{-8}$
N_2/ITQ-29	$1.366 \cdot 10^{-6}$	$2.882 \cdot 10^{-7}$
CO_2/ITQ-29	$1.164 \cdot 10^{-5}$	$1.018 \cdot 10^{-6}$
O_2/ITQ-29	$1.146 \cdot 10^{-6}$	$1.800 \cdot 10^{-7}$
H_2O/ITQ-29	$9.560 \cdot 10^{-8}$	$9.560 \cdot 10^{-11}$
N_2/MFI	$2.730 \cdot 10^{-6}$	$1.234 \cdot 10^{-6}$
CO_2/MFI	$5.393 \cdot 10^{-5}$	$1.982 \cdot 10^{-5}$
O_2/MFI	$2.003 \cdot 10^{-6}$	$7.387 \cdot 10^{-7}$
H_2O/MFI	$6.703 \cdot 10^{-8}$	$2.234 \cdot 10^{-8}$
N_2/MOR	$1.984 \cdot 10^{-6}$	$7.214 \cdot 10^{-7}$
CO_2/MOR	$1.226 \cdot 10^{-5}$	$4.756 \cdot 10^{-6}$
O_2/MOR	$1.573 \cdot 10^{-6}$	$4.863 \cdot 10^{-7}$
H_2O/MOR	$1.058 \cdot 10^{-7}$	$2.645 \cdot 10^{-8}$

Table S5. Comparison between the multicomponent equilibrium data calculated from molecular simulation and IAST method.

Partial Pressure [Pa]				q Molec. Sim. [mol kg^{-1}] BEA				q IAST [mol kg^{-1}] BEA				q Molec. Sim. [mol kg^{-1}] FAU				q IAST [mol kg^{-1}] FAU			
N_2	CO_2	O_2	H_2O	N_2	CO_2	O_2	H_2O	N_2	CO_2	O_2	H_2O	N_2	CO_2	O_2	H_2O	N_2	CO_2	O_2	H_2O
75000	5000	16834	3166	0.118436	0.086011	0.020923	0.000329	0.119043	0.086088	0.021040	0.000333	0.067088	0.023790	0.013026	0.000456	0.067759	0.023930	0.013109	0.000499
150000	10000	36834	3166	0.223561	0.165428	0.043583	0.000330	0.223797	0.165456	0.043712	0.000316	0.132695	0.047887	0.028460	0.000468	0.134065	0.048255	0.028529	0.000498
75000	10000	11834	3166	0.116033	0.171125	0.014443	0.000344	0.116627	0.171118	0.014526	0.000327	0.067263	0.047954	0.009133	0.000486	0.067838	0.048090	0.009226	0.000501
150000	20000	26834	3166	0.214625	0.325900	0.030756	0.000335	0.215284	0.326285	0.030820	0.000306	0.132779	0.097111	0.020678	0.000468	0.134377	0.097450	0.020860	0.000501
75000	15000	6834	3166	0.113967	0.255141	0.008233	0.000353	0.114293	0.254837	0.008230	0.000322	0.067293	0.072627	0.005289	0.000471	0.067917	0.072484	0.005327	0.000502
150000	30000	16834	3166	0.206180	0.481186	0.018629	0.000364	0.207304	0.481099	0.018721	0.000297	0.132533	0.147686	0.012995	0.000497	0.134692	0.147613	0.013129	0.000503
Partial Pressure [Pa]				q Molec. Sim. [mol kg^{-1}] ITQ-29				q IAST [mol kg^{-1}] ITQ-29				q Molec. Sim. [mol kg^{-1}] MFI				q IAST [mol kg^{-1}] MFI			
N_2	CO_2	O_2	H_2O	N_2	CO_2	O_2	H_2O	N_2	CO_2	O_2	H_2O	N_2	CO_2	O_2	H_2O	N_2	CO_2	O_2	H_2O
75000	5000	16834	3166	0.099396	0.053275	0.018837	0.000312	0.099083	0.053318	0.018713	0.000301	0.167541	0.216426	0.028325	0.000199	0.167999	0.216482	0.028175	0.000181
150000	10000	36834	3166	0.191907	0.104707	0.040268	0.000328	0.191721	0.104997	0.039849	0.000297	0.286234	0.377983	0.053509	0.000181	0.283747	0.377118	0.053059	0.000157
75000	10000	11834	3166	0.098672	0.106784	0.013208	0.000317	0.098347	0.106884	0.013064	0.000301	0.153918	0.405445	0.018412	0.000193	0.154163	0.406260	0.018331	0.000168
150000	20000	26834	3166	0.187829	0.210007	0.028997	0.000334	0.188951	0.210075	0.028680	0.000296	0.249821	0.681169	0.034581	0.000184	0.245600	0.680491	0.034007	0.000139
75000	15000	6834	3166	0.097804	0.160497	0.007562	0.000340	0.097619	0.160519	0.007483	0.000300	0.142975	0.574388	0.009986	0.000190	0.142298	0.575397	0.009838	0.000157
150000	30000	16834	3166	0.183302	0.313249	0.017854	0.000341	0.186236	0.313216	0.017769	0.000295	0.219974	0.921248	0.019260	0.000178	0.215942	0.921512	0.019033	0.000125
Partial Pressure [Pa]				q Molec. Sim. [mol kg^{-1}] FER				q IAST [mol kg^{-1}] FER				q Molec. Sim. [mol kg^{-1}] MOR				q IAST [mol kg^{-1}] MOR			
N_2	CO_2	O_2	H_2O	N_2	CO_2	O_2	H_2O	N_2	CO_2	O_2	H_2O	N_2	CO_2	O_2	H_2O	N_2	CO_2	O_2	H_2O
75000	5000	16834	3166	0.081683	0.079185	0.015713	0.000126	0.081931	0.079435	0.015748	0.000106	0.138624	0.056895	0.024861	0.000306	0.137033	0.057128	0.024479	0.000316
150000	10000	36834	3166	0.143100	0.136988	0.030600	0.000127	0.142960	0.136122	0.030353	0.000091	0.254459	0.105702	0.050046	0.000292	0.253587	0.105431	0.049914	0.000296
75000	10000	11834	3166	0.076691	0.147882	0.010456	0.000122	0.076838	0.147836	0.010411	0.000099	0.136637	0.111903	0.017171	0.000312	0.134517	0.112089	0.016901	0.000311
150000	20000	26834	3166	0.129291	0.243012	0.020156	0.000120	0.128597	0.241786	0.020010	0.000080	0.245969	0.203359	0.035452	0.000299	0.245127	0.203595	0.035227	0.000288
75000	15000	6834	3166	0.072479	0.208302	0.005675	0.000127	0.072413	0.207475	0.005674	0.000092	0.135144	0.165497	0.009815	0.000314	0.132094	0.165006	0.009577	0.000306
150000	30000	16834	3166	0.117906	0.328434	0.011643	0.000118	0.117156	0.326738	0.011494	0.000072	0.239163	0.295514	0.021779	0.000301	0.237230	0.295223	0.021424	0.000280

Table S6. Fitted Langmuir parameters in MFI structure.

Parameter	Value
K_{H0} N_2, mol kg^{-1} Pa^{-1}	$3.230 \cdot 10^{-9}$
b_0 N_2, Pa^{-1}	$1.330 \cdot 10^{-9}$
$-\Delta H$ N_2, kJ mol^{-1}	16.65
K_{H0} CO_2, mol kg^{-1} Pa^{-1}	$5.640 \cdot 10^{-10}$
b_0 CO_2, Pa^{-1}	$2.000 \cdot 10^{-10}$
$-\Delta H$ CO_2, kJ mol^{-1}	28.32
K_{H0} O_2, mol kg^{-1} Pa^{-1}	$3.914 \cdot 10^{-9}$
b_0 O_2, Pa^{-1}	$1.515 \cdot 10^{-9}$
$-\Delta H$ O_2, kJ mol^{-1}	15.46
K_{H0} H_2O, mol kg^{-1} Pa^{-1}	$3.621 \cdot 10^{-9}$
b_0 H_2O, Pa^{-1}	$1.448 \cdot 10^{-9}$
$-\Delta H$ H_2O, kJ mol^{-1}	7.25

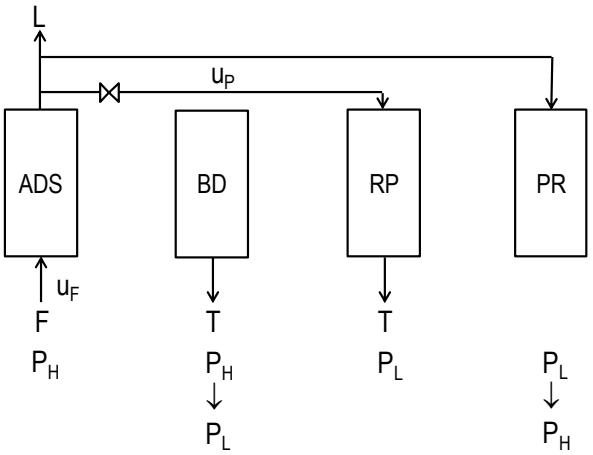

Duration, s	60	100	60	100
COLUMN I	ADS	BD	RP	PR
COLUMN II	RP	PR	ADS	BD

Figure S3. PSA cycle for comparing separation performance. F = feed gas, L = light product, T = tail gas, PH = high pressure, PL = low pressure, ADS = feed gas adsorption, BD = blowdown, RP = receive purge, PR = pressurization, uF = feed gas velocity in the adsorption step, uP = feed gas velocity in the purge step.

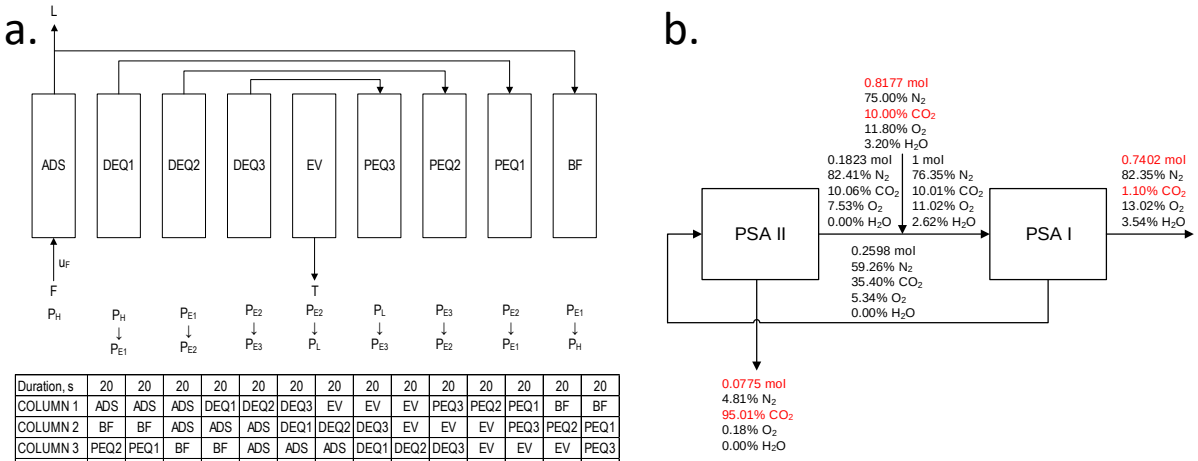

Duration, s	20	20	20	20	20	20	20	20	20	20	20	20	20	20
COLUMN 1	ADS	ADS	ADS	DEQ1	DEQ2	DEQ3	EV	EV	EV	PEQ3	PEQ2	PEQ1	BF	BF
COLUMN 2	BF	BF	ADS	ADS	ADS	DEQ1	DEQ2	DEQ3	EV	EV	EV	PEQ3	PEQ2	PEQ1
COLUMN 3	PEQ2	PEQ1	BF	BF	ADS	ADS	ADS	DEQ1	DEQ2	DEQ3	EV	EV	EV	PEQ3
COLUMN 4	EV	PEQ3	PEQ2	PEQ1	BF	BF	ADS	ADS	ADS	DEQ1	DEQ2	DEQ3	EV	EV
COLUMN 5	EV	EV	EV	PEQ3	PEQ2	PEQ1	BF	BF	ADS	ADS	ADS	DEQ1	DEQ2	DEQ3
COLUMN 6	DEQ2	DEQ3	EV	EV	EV	PEQ3	PEQ2	PEQ1	BF	BF	ADS	ADS	ADS	DEQ1
COLUMN 7	ADS	DEQ1	DEQ2	DEQ3	EV	EV	EV	PEQ3	PEQ2	PEQ1	BF	BF	ADS	ADS

Figure S4. (a.) Individual PSA cycle in dual-PSA configuration for capturing CO_2 from a $N_2/CO_2/O_2/H_2O$ mixture. F = feed gas, L = light product, T = tail gas, P_H = high pressure, P_L = low pressure, ADS = feed gas adsorption, DEQi = ith depressurizing equalization, EV = evacuation, PEQi = ith pressurizing equalization, BF = backfill, u_F = feed gas velocity in the adsorption step. (b.) Flowsheet of the dual-PSA cycle for capturing CO2 from a N2/CO2/O2/H2O mixture. PSA I is the rectifying cycle and PSA II is the stripping cycle.

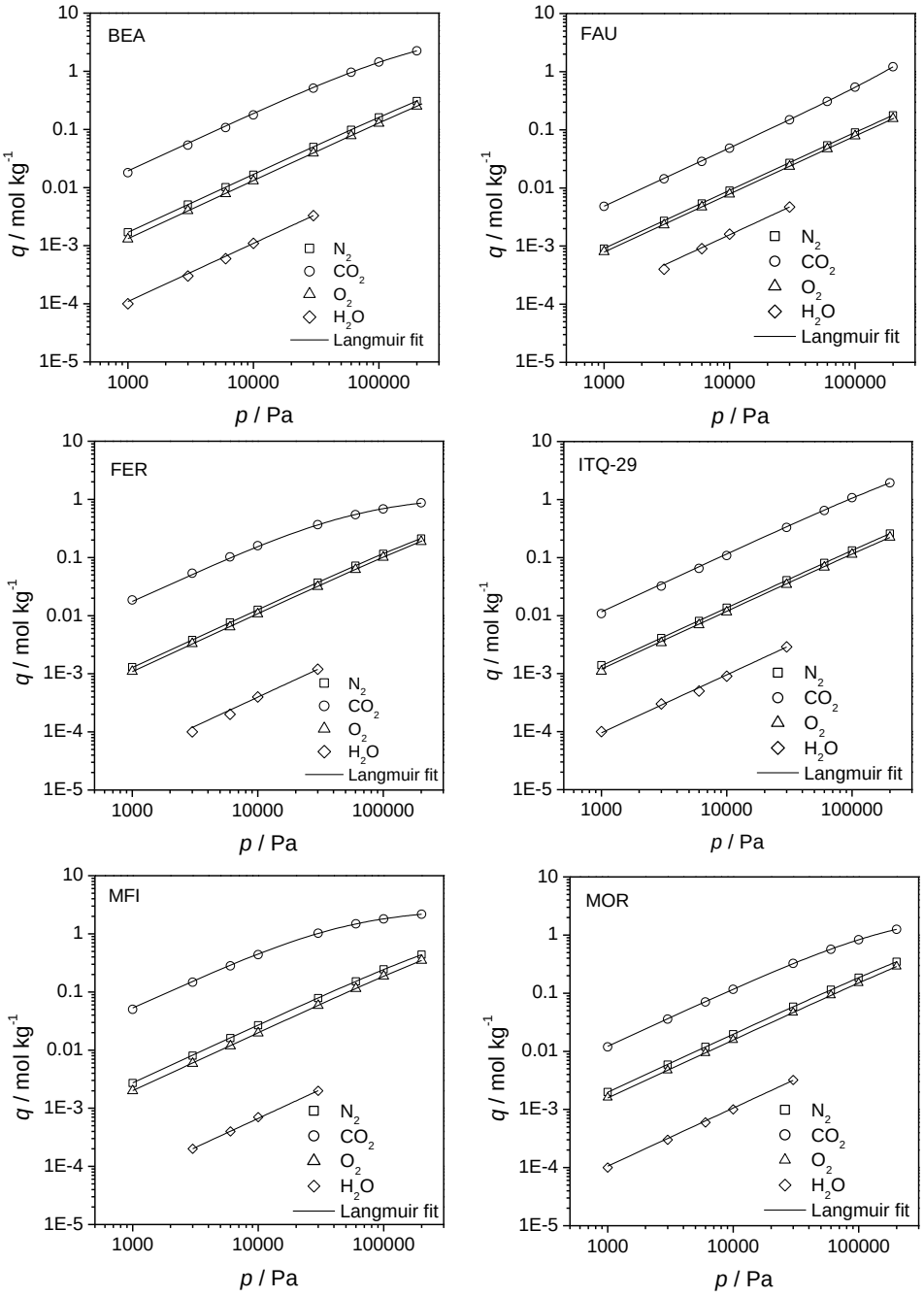

Figure S5. Comparison between pure adsorption isotherms at 298 K obtained by molecular simulation and fitted with Langmuir model.

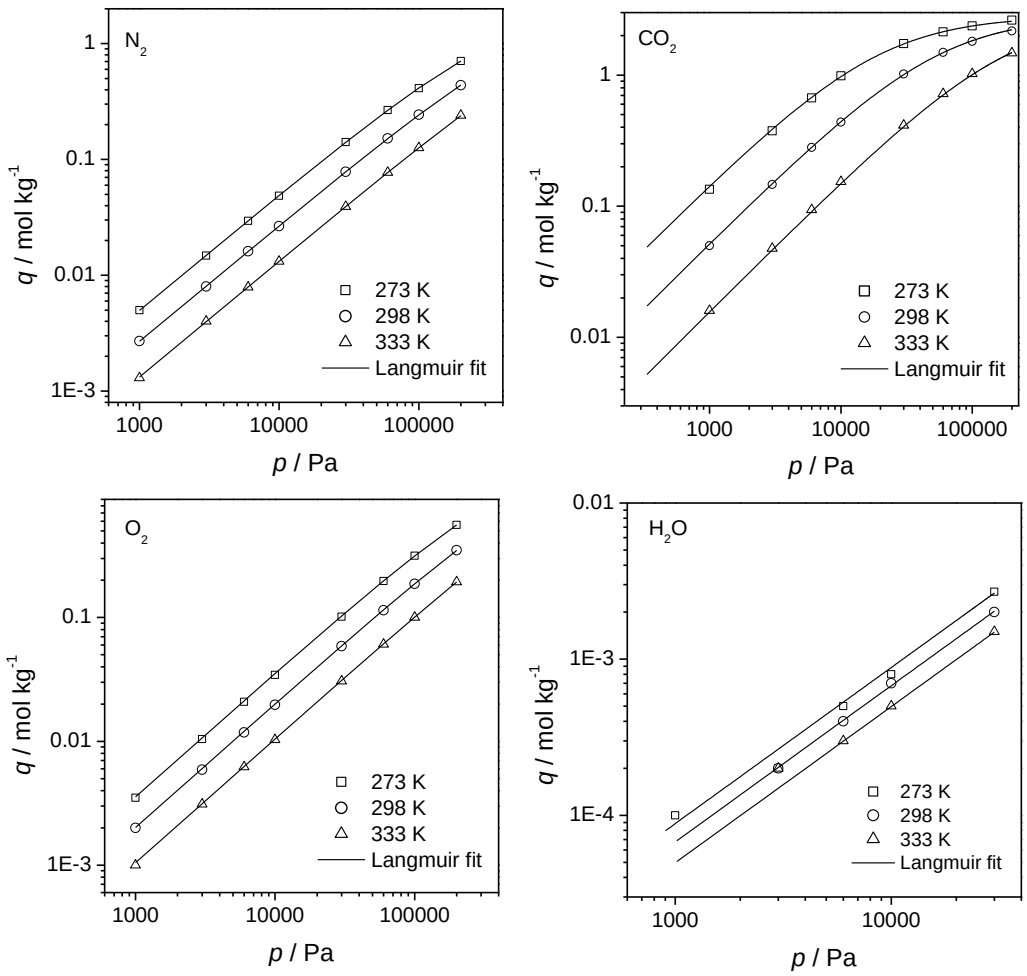

Figure S6. Comparison between pure adsorption isotherms in MFI structure obtained by molecular simulation and fitted with the temperature-dependent Langmuir model.

Section D. Microorganisms and culture media

Table S7.- List of microorganisms selected, including microalgae and cyanobacteria, following the bibliographic revision.

Species	**Microalgae/cyanobacterium**	**Origin**
Scenedesmus almeriensis	Microalga	UAL collection
Neochloris oleoabundans	Microalga	UAL collection
Anabaena sp.	Cyanobacterium	CCAP 1403/13
Spirulina platensis	Cyanobacterium	UAL collection
Nostoc commune	Cyanobacterium	CCAP 1453/33
Calothrix scytonemicola	Cyanobacterium	CCAP 1410/12
Scenedesmus dimorphis	Microalga	UAL collection
Chlorella vulgaris	Microalga	CCAP 211/11D
Monoraphidium griffithii	Microalga	CCAP 202/11D
Synechococcus sp.	Cyanobacteria	CCAP 1479/9

Supplementary results

Figure S7. Average occupation profiles for carbon dioxide (left) and nitrogen (right) in MOR zeolite at room temperature and 10 bar obtained from computed gas mixtures containing CO_2 molar fractions of 0.05 (second file), 0.10 (third file), and 0.15 (fourth file). The figure shows the projection of the center of mass of the molecules over the y-z plane. The color graduation indicates the occupation density (from black –null– to red –high–). To guide the view, a representation of the structure (first file) is added (oxygen atoms are depicted in red and silica atoms in yellow). A grid surface is also represented where the accessible part appears in blue while the non-accessible part is colored in gray.

Figure S8. Average occupation profiles for carbon dioxide in MFI zeolite at room temperature and 1 bar (center-left), 2 bar (center-right), and 10 bar (right), obtained from computed gas mixture. The figures show the projection of the center of mass of the molecules over the z-x (top) and z-y (down) planes. The color graduation indicates the occupation density (from black to red). To guide the view a representation of the structure (first column) is added (oxygen atoms are depicted in red and silica atoms in yellow). A grid surface is also represented where the accessible part appears in blue while the non-accessible part is colored in gray.

Figure S9.- CO_2 fixation rate (A) and biochemical composition (B) of produced biomass of different strains tested at laboratory conditions.

References

1 A. Garcia-Sanchez, C. O. Ania, J. B. Parra, D. Dubbeldam, T. J. H. Vlugt, R. Krishna and S. Calero, *J. Phys. Chem. C*, 2009, **113**, 8814–8820.

2 A. Martin-Calvo, E. Garcia-Perez, A. Garcia-Sanchez, R. Bueno-Perez, S. Hamad and S. Calero, *Phys. Chem. Chem. Phys.*, 2011, **13**, 11165–11174.

3 S. W. Rick, *J. Chem. Phys.*, 2004, **120**, 6085–6093.

4 J. M. Castillo, D. Dubbeldam, T. J. H. Vlugt, B. Smit and S. Calero, *Mol. Simul.*, 2009, **35**, 1067–1076.

5 S. Calero and P. Gómez-Álvarez, *RSC Adv.*, 2014, **4**, 29571.

6 M. P. Allen and D. J. Tildesley, *Computer Simulation of Liquids*, Oxford Clarendon Press, Oxford, Second Edi., 2017.

7 R. Krishna, J. M. van Baten, E. Garcia-Perez and S. Calero, *Ind. Eng. Chem. Res.*, 2007, **46**, 2974–2986.

8 A. Martin-Calvo, J. J. Gutierrez-Sevillano, J. B. Parra, C. O. Ania, S. Calero, J. J. Gutiérrez-Sevillano, J. B. Parra, C. O. Ania and S. Calero, *Phys Chem Chem Phys*, 2015, **17**, 24048–24055.

9 J. M. Castillo, J. Silvestre-Albero, F. Rodriguez-Reinoso, T. J. H. Vlugt and S. Calero, *Phys. Chem. Chem. Phys.*, 2013, **15**, 17374–17382.

10 J. M. Newsam, M. M. J. Treacy, W. T. Koetsier and C. B. D. Gruyter, *Proc. R. Soc. Math. Phys. Eng. Sci.*, 1988, **420**, 375–405.

11 V. Gramlich, Ph.D. Thesis, ETH, Zürich, Switzerland, 1971.

12 E. Garcia-Perez, J. B. Parra, C. O. Ania, A. Garcia-Sanchez, J. M. Van Baten, R. Krishna, D. Dubbeldam and S. Calero, *Adsorpt.-J. Int. Adsorpt. Soc.*, 2007, **13**, 469–476.

13 R. E. Morris, S. J. Weigel, N. J. Henson, L. M. Bull, M. T. Janicke, B. F. Chmelka and A. K. Cheetham, *J. Am. Chem. Soc.*, 1994, **116**, 11849–11855.

14 H. van Koningsveld, H. van Bekkum and J. C. Jansen, *Acta Crystallogr. Sect. B-Struct. Sci.*, 1987, **43**, 127–132.

15 A. Corma, F. Rey, J. Rius, M. J. Sabater and S. Valencia, *Nature*, 2004, **431**, 287–290.

16 J. J. A. Hriljac, M. M. M. Eddy, A. K. K. Cheetham, J. A. A. Donohue and G. J. J. Ray, *J. Solid State Chem.*, 1993, **106**, 66–72.

17 J. A. Delgado, V. I. Águeda, M. A. Uguina, P. Brea and C. A. Grande, *Chem. Eng. J.*, 2017, **326**, 117–129.